Title: Weakening of AMOC linked to past Greenland Ice Sheet retreat

Authors: D. Parkes[1,2]*†, D. Thornalley[2]†, E. McClymont[3]‡, S. Nuber[2]§¶, D. Fairman[2]§, M. Cousins[2]§, A. Palmer[1]‡, I.P. Matthews [1]‡, J. Wharton[2] I. Candy[1]†.

[1]Department of Geography, Royal Holloway, University of London; Egham, TW20 0EX, United Kingdom.

[2]Department of Geography, University College London; London, WC1E 6BT, United Kingdom.

[3]Department of Geography, University of Durham; Durham, DH1 3LE, United Kingdom.

*ucfadre@ucl.ac.uk

†These authors are the primary investigators of this work.

‡These authors assisted in the conception and co-supervision of this work.

§These authors contributed towards data collected in this work.

¶This author is now at University of Washington, U.S.

Title: Weakening of AMOC linked to past Greenland Ice Sheet retreat

Authors: D. Parkes[1,2]*†, D. Thornalley[2]†, E. McClymont[3]‡, S. Nuber[2]§¶, D. Fairman[2]§, M. Cousins[2]§, A. Palmer[1]‡, I.P. Matthews [1]‡, J. Wharton[2] I. Candy[1]†.

Affiliations:

[1]Department of Geography, Royal Holloway, University of London; Egham, TW20 0EX, United Kingdom.

[2]Department of Geography, University College London; London, WC1E 6BT, United Kingdom.

[3]Department of Geography, University of Durham; Durham, DH1 3LE, United Kingdom.

*ucfadre@ucl.ac.uk

†These authors are the primary investigators of this work.

‡These authors assisted in the conception and co-supervision of this work.

§These authors contributed towards data collected in this work.

¶This author is now at University of Washington, U.S.

Abstract: A weakening of the Atlantic Meridional Overturning Circulation (AMOC) is predicted to occur under multiple scenarios of future warming. However, the effect of meltwater from a decaying Greenland Ice Sheet (GrIS) on AMOC is uncertain. Using a basin-wide network of North Atlantic sediment cores, we show that the largescale melting of the GrIS during a previous interglacial (Marine Isotope Stage 11c (MIS11c); 397 – 427 ka) led to a millennial-scale, 30±15% weakening of AMOC and an associated abrupt 2 – 7°C cooling event over the subpolar North Atlantic. Furthermore, we reveal that this AMOC weakening occurred due to a combination of an abrupt transient weakening of Iceland Scotland Overflow Water and a preceding long-term decline in the strength of Denmark Straits Overflow Water, as well as an earlier cooling of the western subpolar gyre. Paleoclimate datasets indicate that this re-arrangement of ocean circulation had an impact on terrestrial ecosystems and atmospheric/oceanic circulation across the northern hemisphere and the low latitudes. This study suggests that modern oceanographic conditions are analogous to those prior to the MIS11c AMOC weakening event, with comparable modern rates of GrIS melt to those modelled for MIS11c. Critically, these findings provide empirical evidence that suggests the potential vulnerability of AMOC weakening to GrIS decay.

Main text:

Introduction

Continued global warming will push components of the Earth system closer to tipping points that, if crossed, may trigger abrupt change (1). One of the most widely discussed tipping points is the potential weakening, or even collapse, of the Atlantic Meridional Overturning Circulation (AMOC), caused by freshwater flux into the North Atlantic through increased precipitation and/or and the melting of high latitude sea-ice and glaciers (1–3). Paleoclimate evidence and modelling studies suggest that an AMOC collapse would have major climatic and socioeconomic impacts (4)(5), including strong cooling over much of the Northern Hemisphere, and shifts in rainfall patterns over west Africa and central Asia (6,7). Future AMOC weakening is, thus, a key concern for global policymakers and stakeholders. Researchers have largely focussed their attention on abrupt events during glacial stages (*e.g,* Dansgaard-Oeschger events), which have been related to shifts in the mode of operation of AMOC (8), but as we are presently in an interglacial stage these glacial events are less relevant as analogues for constraining modern/future AMOC behaviour. Thus, it is imperative to also investigate AMOC and its response to forcing during warm climates, such as previous interglacials. In this study, we investigate the response of AMOC and its key components to a period of increased freshwater flux derived from the melting of Greenland Ice Sheet (GrIS) during Marine Isotope Stage 11c.

There is uncertainty regarding both the magnitude and timing of any future weakening or collapse in AMOC (2,3,9,10). Recent studies have proposed that AMOC could collapse by the middle of the 21st century (2,3), but this contrasts with Intergovernmental Panel on Climate Change (IPCC) projections that do not forecast AMOC collapse under any scenario prior to 2100 (11), with medium confidence. These discrepancies may reflect the fact that climate models summarised in the IPCC reports do not accurately represent key ocean features such as overflows (12), and that they could be biased towards stability; thus, underestimating the potential risk of abrupt AMOC change (13,14). Furthermore, models may not accurately represent ice sheet processes, nor do they routinely account for meltwater runoff from the GrIS (15–17), which has recently been found to be melting 20% faster than previously thought (18). Our understanding of the impact of GrIS melt on AMOC also remains poorly constrained: meltwater experiments produce a wide range of estimates for the rate of GrIS melt necessary to impact AMOC strength (*e.g.* 0.005 – 0.1 Sv), further complicated by differing impacts dependent on meltwater spreading pathways (19–22).

Analysis of empirical data derived from intervals of GrIS melt in the geological past can be used to investigate the potential response of AMOC and its components to freshwater release derived from this source. Evidence suggests that the modern GrIS extent was reached ~7000 years ago, with minimal changes between then and the industrial era (20^{th} century) (23,24). Contrastingly, there is evidence from sediment provenance and pollen data which indicate that a major reduction in GrIS extent relative to today occurred during Marine Isotope Stage 11c (MIS 11c: 397,000 – 427,000 years ago) (25,26), when global surface temperatures were ~1°C warmer than the Holocene/present day but with concentrations of atmospheric CO_2 similar to the pre-industrial period (~280 ppmv) (27,28). This period also has the most convincing evidence for an abrupt climate event in northern Europe (29,30) and the North Atlantic (31–33) from any pre-Holocene interglacial. A recent tephra-based correlation between a European varved lake (Marks Tey) and North Atlantic marine sediment core (ODP Site 980) (34) has shown that an abrupt centennial-scale decline in air temperature over northwest Europe was synchronous with a surface ocean cooling in the northeast Atlantic. Furthermore, records from across western and central Europe

104

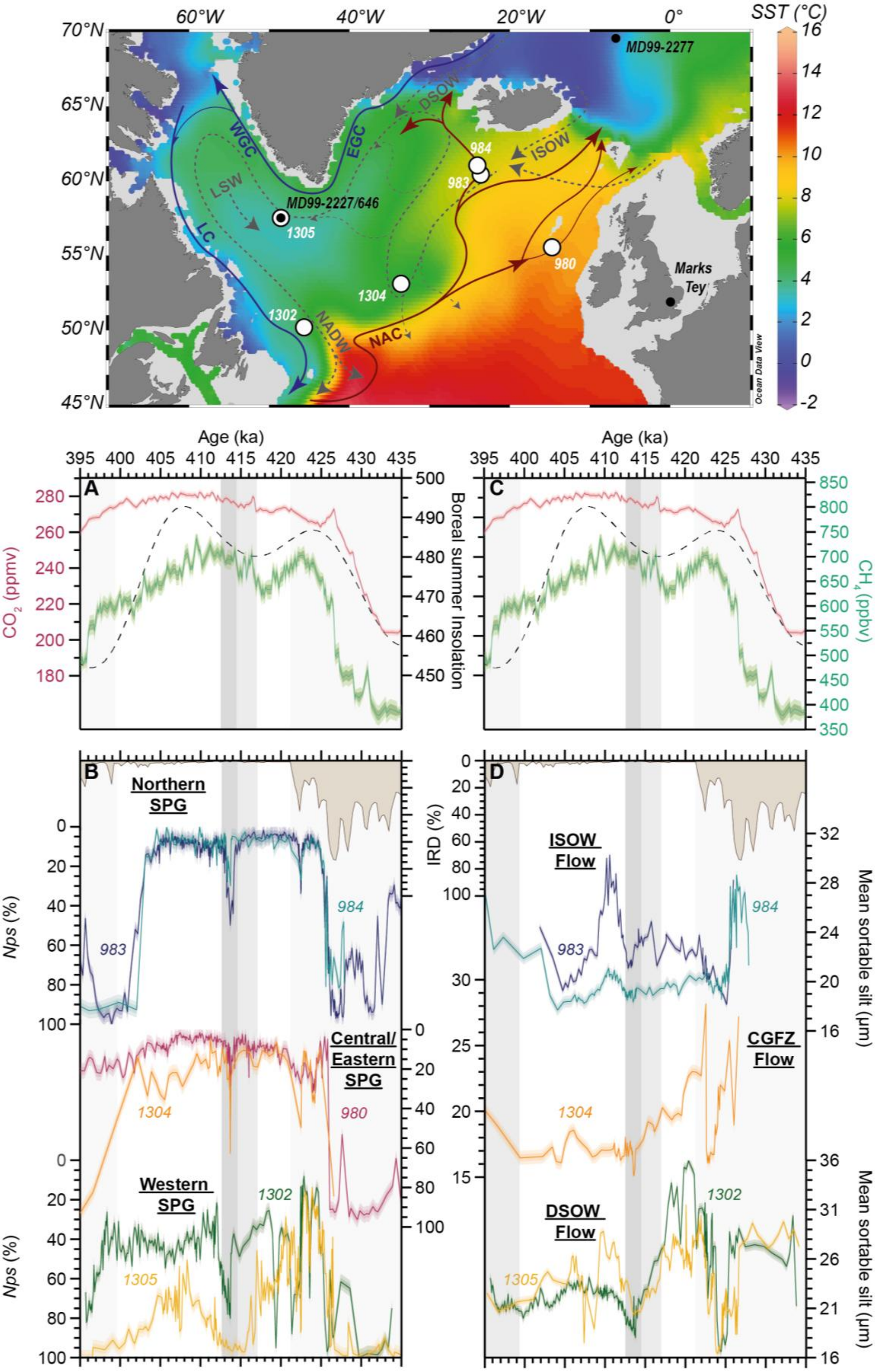

60°W
40°W
20°W
0°
SST (°C)
70°N
65°N
60°N
55°N
50°N
45°N
MD99-2277
WGC
EGC
DSOW
ISOW
LSW
LC
984
983
MD99-2227/646
1305
980
1304
1302
NADW
NAC
Marks Tey
Ocean Data View
16
14
12
10
8
6
4
2
0
-2
Age (ka)
A
B
C
D
CO2 (ppmv)
Boreal summer Insolation
CH4 (ppbv)
Northern SPG
Nps (%)
983
984
Central/ Eastern SPG
1304
980
Western SPG
1302
1305
IRD (%)
ISOW Flow
CGFZ Flow
DSOW Flow
Mean sortable silt (μm)

Fig. 1. Core locations and data synthesis compared to key climate forcings: *(Top) IODP Site U1302 (50.2°N, 45.6°W; 3250m depth) (this study); IODP Site U1305 (57.5°N, 48.5°W; 3463m depth) (this study, (36); ODP Site 983 (60.4°N, 23.6°W; 1983m depth) (this study, (33); ODP Site 984 (61.0°N, 24.0°W; 1650m depth) (this study); IODP Site U1304 (53.1°N, 33.5°W; 3024m depth) (this study); ODP Site 980 (55.5°N, 14.7°W; 2170m depth) (this study, (71); projected on a map of North Atlantic Sea Surface Temperatures (200m depth) using data from WOA18 plotted using Ocean Data View. Study core sites are depicted as white circles with black outlines. Key comparison sites in this study are depicted by black circles. Key surface (solid) and intermediate/deep (dashed) ocean currents are depicted. (**A**, **C**) Key climate forcings (duplicated above each dataset) including greenhouse gas data (CO_2 and CH_4) from EPICA Dome C (28) and summer insolation data at July 65°N (72). (**B**) % Neogloboquadrina pachyderma records compared with compiled normalised Ice Rafted Debris records from study sites. (**D**) Mean sortable silt data compared with a compiled normalised Ice Rafted Debris record from study sites. Coloured bars: grey at onset and end of MIS 11c = ice rafting intervals; light grey = broad mid-interglacial cooling; dark grey = abrupt mid-interglacial cooling.*

show this cooling triggered transformative ecological shifts (30). Currently, it is unclear whether this interglacial cold event was caused by AMOC weakening linked to GrIS melt, and if so, how the surface and deep components of AMOC contributed to the event.

To investigate these questions, palaeoceanographic proxy records were reconstructed using International Ocean Drilling Program (IODP) sites at key locations across the subpolar North Atlantic (see Methods) (Fig. 1). All sites were placed on a common stratigraphic age model via alignment of each site's Relative PalaeoIntensity and benthic foraminiferal oxygen isotope record (see SI). Quantitatively calibrated downcore proxy changes are reported relative to the modern ocean by comparison to modern core top values.

Planktic foraminifera census counts were used to reconstruct upper ocean temperature changes across the subpolar North Atlantic (Fig. 1C). All sites reveal a prominent abrupt cooling event (of 2 – 7°C) centred at ~413 ka, with a longer duration and more severe cooling in the central Labrador Sea, consistent with previous studies (31,33,35,36). This event was not associated with ice rafted detritus, unlike an earlier cold event at ~422 ka, which was associated with the latter stages of the glacial termination (Fig. 1B). It has been proposed that the surface ocean temperature anomaly of the Subpolar Gyre (SPG) region can be used as proxy for AMOC strength (37,38)– AMOC temperature fingerprint (see Methods). Accordingly, we combine our surface ocean temperature records to generate a surface ocean temperature-based record of AMOC strength ($AMOC_{SPG-T}$; Figure 2A). Our $AMOC_{SPG-T}$ record reveals long-term weakening of AMOC from 420 – 413 ka, with a more abrupt weakening centred at ~ 413 ka, representing a 50± 15% decline in AMOC strength from the strongest (+15% relative to modern) to weakest (-35% relative to modern) state during MIS 11c (420 – 413 ka), of which 30% occurred in association with the abrupt weakening at 413 ka. An earlier smaller (~15%) transient weakening also occurred at 417 ka.

Additional evidence for changes in AMOC during the mid-MIS11c cold event is gained by employing the mean sortable silt ($\overline{SS}$) grain size proxy to reconstruct deep water flow speeds at our core sites (Fig. 1D). These sites are located under the pathway of the two major Nordic Overflows, Iceland Scotland Overflow Waters (ISOW) and Denmark Strait Overflow Waters (DSOW) and are used to produce a record of the overall strength of the combined Nordic Overflows. Figure 2A shows that the abrupt weakening recorded by our $AMOC_{SPG-T}$ proxy was accompanied by a 40% weakening (reaching -20% relative to modern strength at its lowest) of the Nordic Overflows from 414 – 413 ka (Fig. 2B). This was preceded by a multi-centennial 15±20% weakening of $AMOC_{NSO}$ event at 417 ka, which occurred against a background of strong Nordic Seas overflows (+40% relative to modern) which was also associated with a weakening in $AMOC_{SPG-T}$. Weakening of AMOC is also suggested by reconstructed declines in benthic $\delta^{13}C$ and $CaCO_3$ preservation in the deep Northwest Atlantic at sites typically bathed by North Atlantic Deep Water (NADW) during interglacials, suggesting the weakening and/or shoaling or NADW (39,40) (Fig. 2C). Therefore, there is evidence of a substantial AMOC weakening during mid-MIS11c from both surface and deep ocean proxy records that persisted for ~1000 years before recovering.

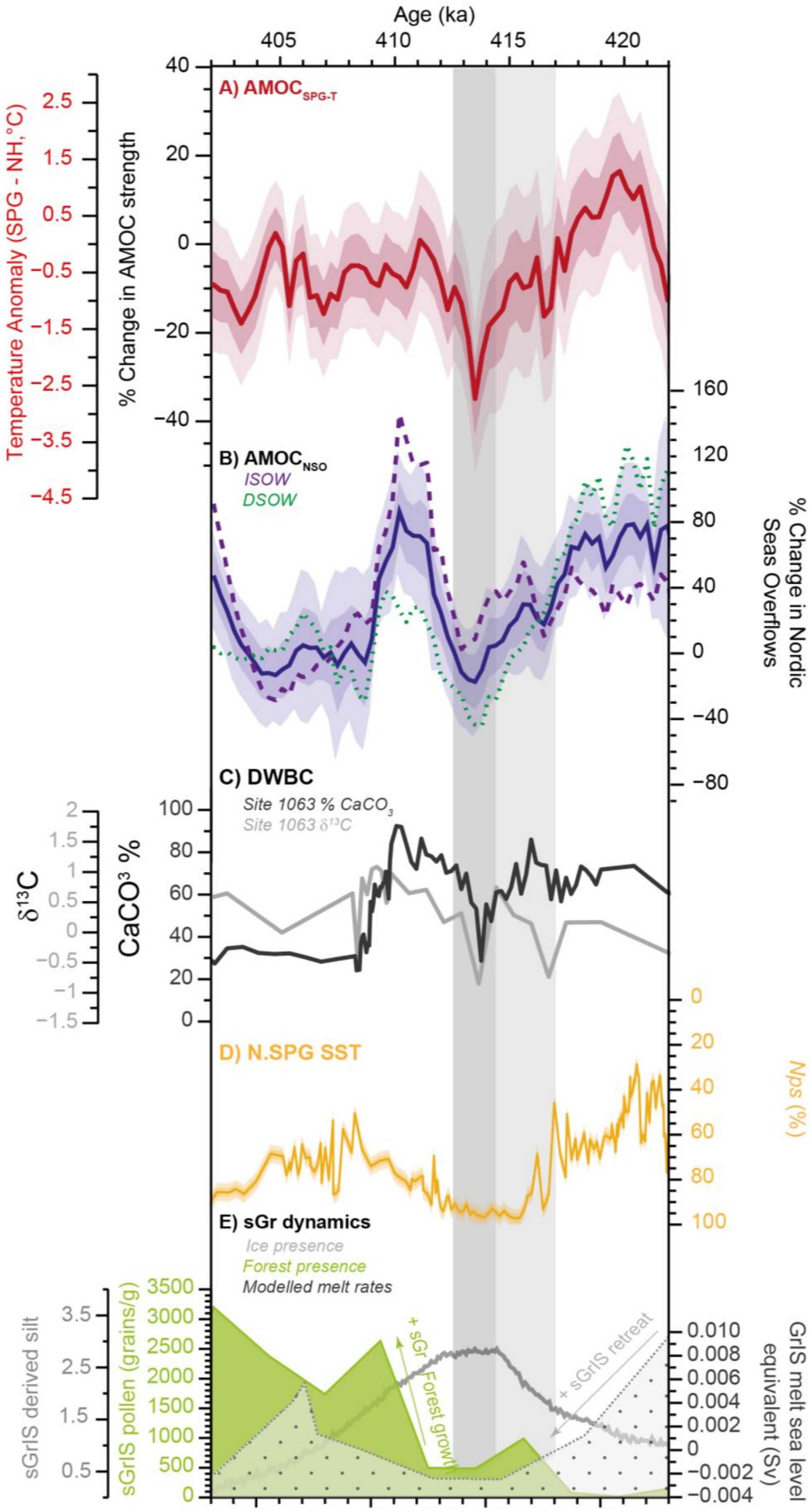
Age (ka)
405
410
415
420
A) AMOC$_{SPG-T}$
Temperature Anomaly (SPG - NH,°C)
% Change in AMOC strength
B) AMOC$_{NSO}$
ISOW
DSOW
% Change in Nordic Seas Overflows
C) DWBC
Site 1063 % $CaCO_3$
Site 1063 $\delta^{13}C$
$\delta^{13}C$
$CaCO^3$ %
D) N.SPG SST
Nps (%)
E) sGr dynamics
Ice presence
Forest presence
Modelled melt rates
+ sGr Forest growth
+ sGrIS retreat
sGrIS derived silt
sGrIS pollen (grains/g)
GrIS melt sea level equivalent (Sv)

Fig. 2. Compiled Nordic Seas overflow records compared to the AMOC index and potential forcing mechanisms during the main interglacial period of MIS 11c: *(**A**) Reconstructed AMOC index ($AMOC_{SPG-T}$) presented as (red) global sea surface temperature anomaly with reference to modern and (black) percent change with reference to modern AMOC (~ 18 Sv) (see Methods for more details). (**B**) Combined Nordic Seas overflow record ($AMOC_{NSO}$) across MIS 11c presented as percent change with reference to modern, assuming an equal contribution of both DSOW and ISOW. ISOW is depicted as a purple dashed line. DSOW is depicted as a green dotted line. Error bars shown for AMO_{NSO} (1σ and 2σ) were generated using a Monte-carlo runs with a 1 cm s^{-1} error attributed, in addition to random perturbations using age tie point uncertainties from this study (see SI) (**C**) Proxy records (Benthic $d^{13}C$ and % $CaCO_3$) of changes in the Deep Western Boundary Current (DWBC) from ODP Site 1063 (39,73). % $CaCO_3$ was calculated using equations from (74). (**D**) Record Sea surface temperature indicator (% N.pachyderma) record from the northern Subpolar Gyre (IODP Site U1305), highlighting the saturation of % N.pachyderma at 417 ka, earlier than other sites (see Fig. 1B), suggesting sea ice formation and reduction in local convective activity. (**E**) Greenland ice sheet dynamics derived from $CaCO_3$-free silt flux (grey dotted polygon) (25) and pollen concentrations (green polygon) (26). Modelled GrIS meltwater flux was derived from Robinson et al. (2017) (see SI) (grey solid line) and has been temporally adjusted within age model uncertainties so that the highest rates of meltwater flux coincide with the smallest sGrIS extent. Note this has been inverted. Coloured bars: light grey = broad mid-interglacial cooling; dark grey = abrupt mid-interglacial cooling.*

Differing behaviour of Nordic Overflows

Before exploring how different individual AMOC components contributed to the minimum in AMOC strength at ~ 413 ka, we first explore and explain the behaviour of each of the Nordic Seas Overflows through MIS11c, and in doing so provide the context necessary for developing a mechanistic understanding of the abrupt MIS11c event (Fig. 3).

Figure 3 presents our $\overline{SS}$ based constraints on the two Nordic Seas overflows, revealing that they exhibited different behaviour during MIS11c, consistent with similar findings from the late Holocene (41) and instrumental period (42). Our data reveal that ISOW was anomalously strong (+ 150±15% relative to modern) during mid-MIS 11c (Fig 3A). Previous Holocene work has shown that ISOW reached a maximum strength once remnant ice sheets had melted away and insolation changes reduced Arctic sea-ice export to the Nordic Seas, thus allowing strong Nordic Seas deep convection. Our new results show similar behaviour during MIS 11c with a prominent maximum in ISOW strength occurring during the later MIS11 maximum in 65°N summer insolation, when proxy data from the Nordic Seas indicate changes in the water column that favour increased convection (43,44), thus promoting stronger ISOW production (Fig 3A, and Methods/SI).

In contrast to ISOW, DSOW was anomalously strong (+130%±30% relative to modern) during early MIS11c (423 – 417 ka; Fig 3B). We propose that this was due to the effects of the remnant Laurentide Ice Sheet (LIS) on (i) atmospheric circulation, and (ii) surface ocean density gradients. Model simulations show that a remnant LIS can promote more northerly winds in the western Nordic Seas (45), which have been linked to a stronger flow of water along the Greenland margin that feeds directly into, and strengthens, DSOW (41). Equally, model simulations have also shown that increased meltwater derived from the decaying LIS can reduce the density of the upper ocean in the Labrador and Irminger Seas, thus increasing the density gradient across the Denmark Strait and driving a stronger DSOW (46). The result of these two factors would be a substantially strengthened DSOW during greater LIS extent which gradually weakens to modern values as the LIS retreats, in agreement with the proxy data (Fig. 3B).

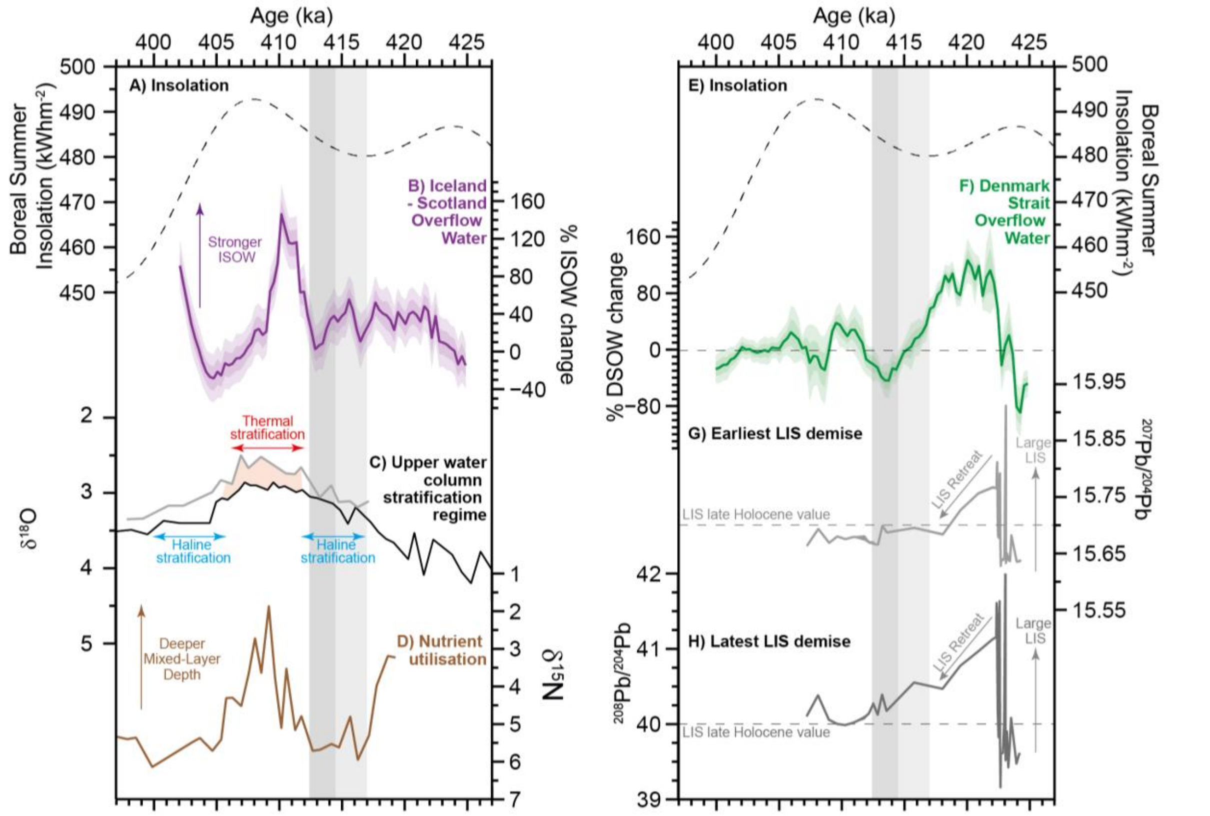

Fig. 3. Records of Nordic Seas overflows compared to key forcings across MIS 11c: *(75). (**A-D**) Compiled ISOW record compared to forcing mechanisms. **(A):** Boreal summer insolation was obtained from (72). **(B):** Compiled ISOW record (purple) derived from Sites 983 and 984 **(C):** Oxygen isotopes derived from planktic foraminifera N.pachyderma (black) and T.quinqueloba (grey) (76). Highlighted in red are consistent (multi-datapoint) offsets of ≥0.4‰, indicating a thermal regime, favouring increased convection and stronger ISOW. **(D):** Nitrate utilisation (^{15}N) indicates reduced utilisation during the mid-late interglacial, indicating increased mixed-layer depth, favouring convection (43); (**E-H**) Compiled DSOW record compared to forcing mechanisms. **(E):** Boreal summer insolation was derived from (72). **(F):** Compiled DSOW record from Sites U1302 and U1305 (green); **(G-H):** Lead isotope data indicates the earliest **(G)** and latest **(H)** timing of the Laurentide Ice Sheet retreating to the late Holocene extent (Canadian Archipelago) on the age model of this study (late Holocene levels = dashed line). The larger Laurentide Ice Sheet coincides with strongest DSOW. All records are presented relative to their modern values (WOCE SSTs and modern coretop mean sortable silt values). Error bars shown for DSOW and ISOW (1σ and 2σ) were generated using a Monte-carlo runs with a 1 cm s^{-1} error attributed, in addition to random perturbations using age tie point uncertainties from this study (see SI). Coloured bars: light blue = broad mid-interglacial AMOC weakening; dark blue = abrupt mid-interglacial AMOC weakening.*

Contributions to AMOC weakening

Next, we explore the contribution of ISOW and DSOW to AMOC weakening during mid-MIS 11c (Figure 2A). Figure 3A shows that there were two transient ISOW weakening events at 417 – 415 and 414 – 412 ka (each of approximately 40%). In isolation, neither event was sufficient to drastically weaken overall AMOC strength; rather, it is because these events occurred in addition to a long term (418 – 412 ka) decrease of 150±15% in DSOW strength (Fig. 3B), which culminated in the overall minimum (-20±30% compared to modern) in combined Nordic Overflow strength during the latter ISOW event at 413 ka (Fig. 2B).

Another clear difference in the climate state between the two ISOW weakening events is the spatial extent of surface ocean cooling. An abrupt, large (7±1.5°C), and persistent cooling of the north-western SPG (Labrador Sea; Fig 3D) occurred at 417 ka which, based on the high % *Nps* values, was likely associated with increased sea-ice cover; but this was spatially restricted to the western SPG region, as southern-SPG and central/eastern subpolar North Atlantic sites maintained low abundance of the polar foraminifera *Nps* at this time. In contrast, cooling extended across the whole of the subpolar North Atlantic from 414 – 412 ka (*i.e.*, during the second interval of ISOW weakening). These spatial surface ocean temperature patterns closely resemble those expected for, respectively, a collapse of subpolar convection (associated with weakened formation of water in the subpolar North Atlantic, today termed Labrador Sea Water (LSW)), versus the more extensive cooling simulated for a more severe AMOC weakening caused by the reduction of the Nordic Seas overflows (47).

Consequently, the broader AMOC weakening interval from 417 ka to 412 ka can be subdivided into: (i) an initial stage (417 – 415 ka) involving a transient weakening of ISOW and a collapse of subpolar convection (and by inference LSW weakening), with cooling and expansion of sea-ice extent limited to the Labrador Sea region; and (ii) a second stage (414 – 412 ka) characterized by widespread cooling of the entire subpolar North Atlantic linked to a further, more severe weakening of AMOC caused by the combined effect of a now much weaker DSOW and a transient ISOW weakening.

Weakening of AMOC during enhanced GrIS melt

In addition to revealing that there was a decline in both the Nordic Seas overflows and overall AMOC strength at 414 – 412 ka (Fig. 3A and 3B), we are able to directly align our records of this event on the same timescale as the proxy records that reconstruct southern GrIS melt and retreat (Fig. 3E). Previous work has used pollen records from Atlantic marine cores to indicate GrIS deglaciation through the rapid development of spruce forest in southern Greenland at this time (26). This has been supported by silt provenance data from similar archives to reconstruct shifts in erosion patterns and, consequently, to infer a retreat of the southern GrIS. Stratigraphic alignment of the respective cores enables us to show that the reconstructed period for AMOC weakening coincided with this inferred melting of the Southern GrIS, and the subsequent rapid expansion of woodland in the region.

The maximum modelled rate of GrIS meltwater flux during MIS 11c was ~ 0.008 – 0.01 Sv (Fig. 3E), which is at the lower end of the estimated flux required to impact AMOC, according to modelling studies investigating AMOC weakening (19–22). Furthermore the GrIS flux estimates from MIS 11c are substantially lower than the rate of freshwater flux currently occurring (0.04 Sv) (48). Previous work has suggested that a meltwater flux of 0.01 Sv is sufficient to weaken Labrador Sea convection if it persisted over a sustained period (21), and present day meltwater fluxes are exceeding this and have been argued to be impacting Labrador Sea convection (49). What is less certain is the impact of GrIS melt on DSOW in the future as this is not as routinely investigated by ocean models. This is critical as, during MIS 11c, the weakening of DSOW appears to have been a key contributor to the occurrence of the severe AMOC weakening at 413 ka.

Despite model experiments suggesting that there would have been continued, prolonged melting of the GrIS, our data show that AMOC did not remain in a weakened state for the rest of the interglacial, but instead the weak AMOC event persisted for ~1000 years before recovering to pre-event levels (and stronger for the Nordic Overflows; Fig 2B)). This AMOC recovery is consistent with model results from abrupt CO_2 forcing scenarios where AMOC recovers on multi-centennial to millennial timescales (50) as well as the transient nature of the Holocene 8.2 kilo-year event (40).

Are we poised to experience an AMOC event similar to during MIS11c? Through a comparison of the downcore data to modern (core-top) conditions, our data reveal that conditions today bear close resemblance to those that occurred prior to the weak AMOC event at 413 ka, namely: (i) ISOW has weakened throughout the mid-late Holocene (51) and it is at a similar strength now as at 414 - 412 ka; (ii) the relative abundance of polar planktic foraminifera in the northwest SPG (Labrador Sea) region (and the broader basin-wide spatial pattern of upper ocean temperatures), today, is comparable to that recorded after the SPG shift at 417 ka and prior to the AMOC weakening event at 413 ka (Fig. 3c); and (iii) the present-day GrIS surface mass-balance anomaly is comparable to modelled meltwater flux rates during MIS11c, and are increasing (18). The key difference between conditions prior to the abrupt mid-MIS 11c AMOC event and today is that, to our knowledge, there is no evidence reporting a significant long-term (i.e. beyond inter-annual to decadal) weakening of DSOW, which our data suggest was a key component of the MIS11c AMOC weakening (see SI). Of concern are observations showing a recent short-term decline in the Deep Western Boundary Current transport along the eastern flank of Greenland, by 26% from 2014 to 2020, due to thinning of the mixed layer and weakening velocities (18,52). Based on evidence from MIS11c, it is important that we continue to monitor the changing strength of DSOW.

Climatic impacts of AMOC weakening during MIS 11c

Modelling studies have demonstrated that any future weakening of the AMOC will have global climate consequences (4)(5). Beyond its effect on North Atlantic conditions, simulations predict that an AMOC slowdown would significantly impact temperatures and precipitation patterns across Europe and West Africa and affect monsoon intensity in Asia (4). These shifts would trigger substantial socioeconomic impacts, including changes in wildfire magnitude and frequency, as well as agricultural productivity (4). As the scale of AMOC weakening identified in this study during MIS 11c (30-50%) is comparable to that predicted under future warming scenarios (12 – 54%) (53), the climate impacts of our MIS11c AMOC weakening event should be detectable in appropriate palaeoclimate archives elsewhere in the world.

A review of palaeoenvironmental archives that span MIS 11c indicate that evidence for climatic instability coincident with our evidence for AMOC weakening is widespread across a range of locations worldwide. This includes evidence for cooling and/or aridification in both northern and southern Europe (Fig. 4A and 4C), reductions in SST from marine cores of the Atlantic margins of southwest Europe and west Africa (Fig. 4E and 4F) and weakening of the strength of the Asian monsoon (Fig. 4D). In many of these regions there is demonstratable evidence for ecological disruption in association with this instability (35). The timing of our reconstruction of the onset of broad AMOC weakening is also coincident with an abrupt short-lived increase in atmospheric CO_2 concentrations (a carbon dioxide jump, or CDJ) (Fig. 4H). It has been postulated that the CDJ within MIS 11c is a result of large-scale disruption of AMOC during this interglacial (28) and our findings would support this, though it is notable no such similar increase occurred during maximum MIS 11c AMOC weakening. In summary, the weakening of AMOC during MIS 11c is accompanied by widespread climate instability which is consistent with the findings of studies that model the impact of future weakening/shutdown of AMOC.

278

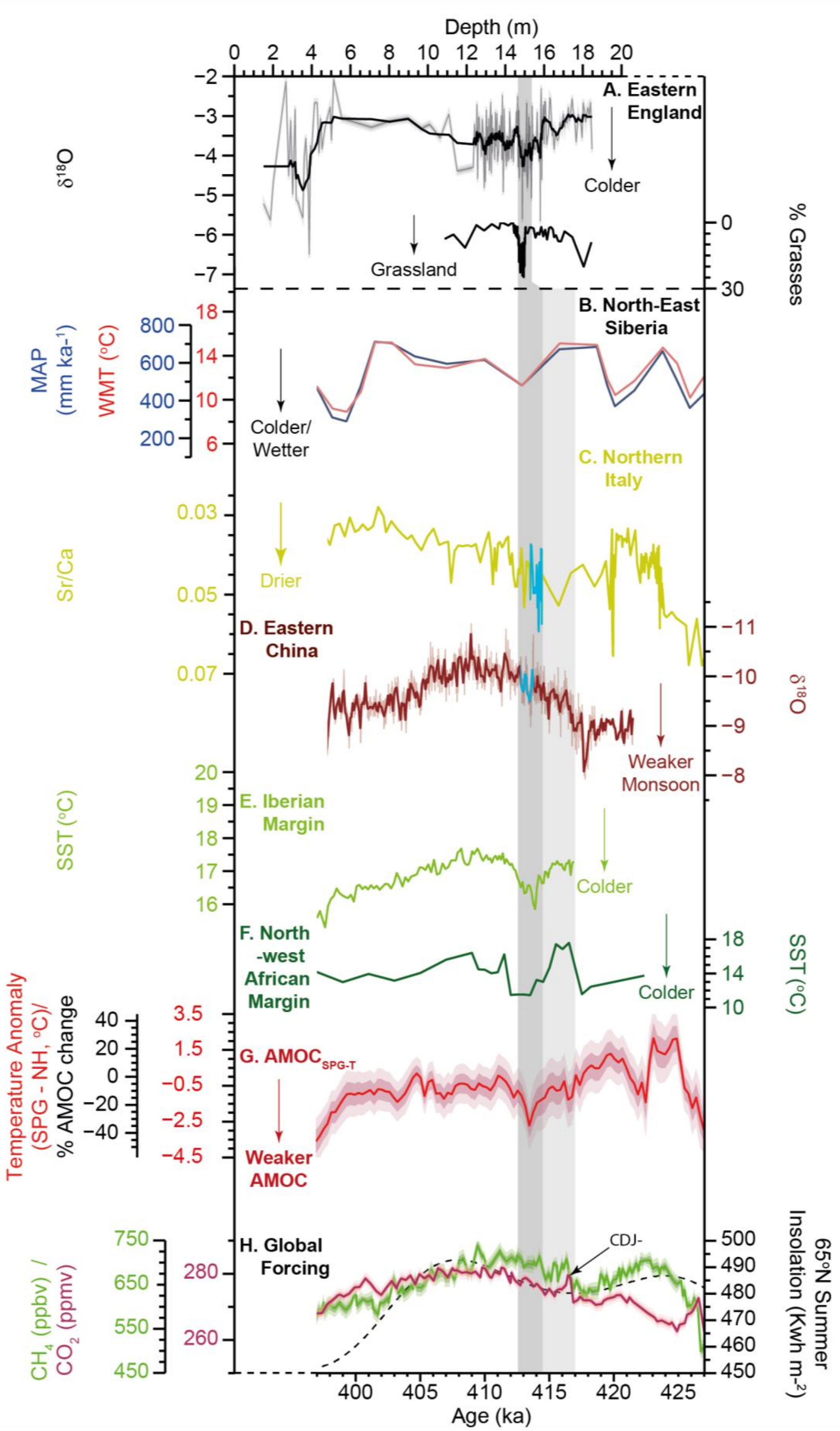
Depth (m)
A. Eastern England
δ18O
Colder
Grassland
% Grasses
B. North-East Siberia
MAP (mm ka-1)
WMT (°C)
Colder/ Wetter
C. Northern Italy
Sr/Ca
Drier
D. Eastern China
δ18O
Weaker Monsoon
E. Iberian Margin
SST (°C)
Colder
F. North-west African Margin
SST (°C)
Colder
Temperature Anomaly (SPG - NH, °C)/ % AMOC change
G. AMOC SPG-T
Weaker AMOC
H. Global Forcing
CH4 (ppbv) / CO2 (ppmv)
CDJ-
65°N Summer Insolation (Kwh m-2)
Age (ka)

Fig. 4. Global comparison of key MIS 11c records that show evidence for mid-interglacial instability associated with AMOC weakening: *(**A**) Temperature and key vegetational data from Marks Tey palaeolake, Northwestern Europe. Oxygen isotope data from authigenic calcite laminations indicating changes in summer air temperature (29). Solid black line = 11.pt running mean; translucent grey line = raw data. Error is 1σ = 0.09; compared with percentage change in grass pollen (29), with increasing percentages indicating an open landscape (note reversed axis). Data from Marks Tey has been aligned to the study age model using the age of the tephra layer at ODP Site 980 (34). Note that Marks Tey data is presented on depth as just the varved section (~ 12 – 16) has robust chronological control, whilst the rest of the sequence does not have a known sedimentation rate. **(B)**: Pollen-based temperature (red) and precipitation (blue) reconstructions from North-east Siberia (77). WMT = Warmest month temperature; MAP = Mean annual precipitation. Error bars show highest and lowest values. (**C**) Strontium Calcium ratios from Bàsuru Cave speleothem record, Northern Italy (78). Higher values (note reversed axis) indicate cooler, drier conditions. (**D**) Oxygen isotope data from Yongxing Cave speleothem record from Eastern China. Higher values (note reversed axis) indicate weaker Asian Summer Monsoon (79). Blue lines for both B and C are the suggested equivalent of the mid-MIS 11c severe AMOC weakening and have been highlighted due to the high variability in these records (**E**) Alkenone ($U^{k}_{37'}$) derived Sea Surface Temperature record of MIS 11c from Site MD01-2443 (37.9°N, 10.2°W; water depth 2925m), Iberian margin, on the age model of this study (44). (**F**) Faunal (Modern Analogue Technique) Sea Surface Temperature record of MIS 11c from ODP Site 958 (24.0°N, 20.0°W; water depth 3728m), North-west African margin, on the age model of this study (80). (**G**) $AMOC_{SPG-T}$ presented as a comparison to global records of MIS 11c. (**H**) Global climate forcings including Carbon dioxide (red), methane (green) (28) and insolation (dashed black) (72). Light blue shading indicates broad AMOC weakening, dark blue shading indicates abrupt AMOC weakening. Dashed blue line from top to bottom indicates the potential equivalent stratigraphic positions of the onset of AMOC weakening at ~ 417 ka in this study, marked by the CDJ- event in panel F. Note that the greenhouse gas concentrations are on AICC2023 (81), as is the data from this study.*

MIS 11c AMOC weakening: a lesson for the future?

AMOC is a crucial component of the climate system, but its response to ongoing and projected GrIS melting is uncertain. Our study has shown that a 30±15% mid-interglacial weakening of AMOC occurred during MIS 11c, with associated shifts in the global climate system. Moreover, our data reveal that this AMOC weakening event occurred during the most substantial wastage of the GrIS of the past 500,000 years. We propose that GrIS melt was causally responsible for the AMOC weakening. There is wide debate about when or if GrIS melting may cause AMOC weakening. Our study indicates that AMOC may respond to GrIS wastage even when melt rates are relatively low (0.01 Sv or less). Furthermore, we find that conditions today bear close resemblance to those prior to the mid-MIS 11c AMOC weakening. In MIS 11c, a substantial weakening of DSOW was a key factor contributing to the weak AMOC event, highlighting the need to correctly understand, monitor and model this AMOC component. Based on the analogy of events during MIS11c as revealed by our study, if present rates of GrIS melt continue, we should expect AMOC to weaken and for that weakening to have far reaching impacts on the Earth system.

References

1. Armstrong McKay DI, Staal A, Abrams JF, Winkelmann R, Sakschewski B, Loriani S, et al. Exceeding 1.5°C global warming could trigger multiple climate tipping points. Science. 2022 Sep 9;377(6611):eabn7950.

2. van Westen RM, Kliphuis M, Dijkstra HA. Physics-based early warning signal shows that AMOC is on tipping course. Science Advances. 2024 Feb 9;10(6):eadk1189.

3. Ditlevsen P, Ditlevsen S. Warning of a forthcoming collapse of the Atlantic meridional overturning circulation. Nat Commun. 2023 Jul 25;14(1):4254.

4. Jackson LC, Kahana R, Graham T, Ringer MA, Woollings T, Mecking JV, et al. Global and European climate impacts of a slowdown of the AMOC in a high resolution GCM. Clim Dyn. 2015 Dec 1;45(11):3299–316.

5. Liu W, Fedorov AV, Xie SP, Hu S. Climate impacts of a weakened Atlantic Meridional Overturning Circulation in a warming climate. Science Advances. 2020 Jun 26;6(26):eaaz4876.

6. Yu T, Cheng J, Lin P, Yu Y, Guo P. Responses and mechanisms of East Asian winter and summer monsoons to weakened Atlantic meridional overturning circulation using the FGOALS-g2 model. International Journal of Climatology. 2018;38(5):2618–26.

7. Sun Y, Clemens SC, Morrill C, Lin X, Wang X, An Z. Influence of Atlantic meridional overturning circulation on the East Asian winter monsoon. Nature Geosci. 2012 Jan;5(1):46–9.

8. Thornalley DJR, Barker S, Becker J, Hall IR, Knorr G. Abrupt changes in deep Atlantic circulation during the transition to full glacial conditions. Paleoceanography. 2013;28(2):253–62.

9. Boers N. Observation-based early-warning signals for a collapse of the Atlantic Meridional Overturning Circulation. Nat Clim Chang. 2021 Aug;11(8):680–8.

10. Chen X, Tung KK. Evidence lacking for a pending collapse of the Atlantic Meridional Overturning Circulation. Nat Clim Chang. 2024 Jan;14(1):40–2.

11. Intergovernmental Panel On Climate Change (Ipcc). Climate Change 2022 – Impacts, Adaptation and Vulnerability: Working Group II Contribution to the Sixth Assessment Report of the Intergovernmental Panel on Climate Change [Internet]. 1st ed. Cambridge University Press; 2023 [cited 2023 Nov 28]. Available from: https://www.cambridge.org/core/product/identifier/9781009325844/type/book

12. Hirschi JJM, Barnier B, Böning C, Biastoch A, Blaker AT, Coward A, et al. The Atlantic Meridional Overturning Circulation in High-Resolution Models. Journal of Geophysical Research: Oceans. 2020;125(4):e2019JC015522.

13. Hofmann M, Rahmstorf S. On the stability of the Atlantic meridional overturning circulation. Proceedings of the National Academy of Sciences. 2009 Dec 8;106(49):20584–9.

14. Jackson LC, Hewitt HT, Bruciaferri D, Calvert D, Graham T, Guiavarc'h C, et al. Challenges simulating the AMOC in climate models. Philosophical Transactions of the Royal Society A: Mathematical, Physical and Engineering Sciences. 2023 Oct 23;381(2262):20220187.

15. Randall DA, Wood RA, Bony S, Colman R, Fichefet T, Fyfe J, et al. Climate models and their evaluation. In: Climate change 2007: The physical science basis Contribution of Working Group I to the Fourth Assessment Report of the IPCC (FAR) [Internet]. Cambridge University Press; 2007 [cited 2024 Apr 7]. p. 589–662. Available from: https://pure.mpg.de/rest/items/item_1765216/component/file_1765214/content

16. Bindschadler RA, Nowicki S, Abe-Ouchi A, Aschwanden A, Choi H, Fastook J, et al. Ice-sheet model sensitivities to environmental forcing and their use in projecting future sea level (the SeaRISE project). Journal of Glaciology. 2013 Jan;59(214):195–224.

17. Pontes GM, Menviel L. Weakening of the Atlantic Meridional Overturning Circulation driven by subarctic freshening since the mid-twentieth century. Nat Geosci. 2024 Nov 18;1–8.

18. Greene CA, Gardner AS, Wood M, Cuzzone JK. Ubiquitous acceleration in Greenland Ice Sheet calving from 1985 to 2022. Nature. 2024 Jan;625(7995):523–8.

19. Swingedouw D, Rodehacke CB, Olsen SM, Menary M, Gao Y, Mikolajewicz U, et al. On the reduced sensitivity of the Atlantic overturning to Greenland ice sheet melting in projections: a multi-model assessment. Clim Dyn. 2015 Jun 1;44(11):3261–79.

20. Swingedouw D, Houssais MN, Herbaut C, Blaizot AC, Devilliers M, Deshayes J. AMOC Recent and Future Trends: A Crucial Role for Oceanic Resolution and Greenland Melting? Frontiers in Climate [Internet]. 2022 [cited 2023 Dec 4];4. Available from: https://www.frontiersin.org/articles/10.3389/fclim.2022.838310

21. Schulz M, Prange M, Klocker A. Low-frequency oscillations of the Atlantic Ocean meridional overturning circulation in a coupled climate model. Climate of the Past. 2007 Feb 7;3(1):97–107.

22. Sinet S, von der Heydt AS, Dijkstra HA. AMOC Stabilization Under the Interaction With Tipping Polar Ice Sheets. Geophysical Research Letters. 2023;50(2):e2022GL100305.

23. Briner JP, McKay NP, Axford Y, Bennike O, Bradley RS, de Vernal A, et al. Holocene climate change in Arctic Canada and Greenland. Quaternary Science Reviews. 2016 Sep 1;147:340–64.

24. Briner JP, Cuzzone JK, Badgeley JA, Young NE, Steig EJ, Morlighem M, et al. Rate of mass loss from the Greenland Ice Sheet will exceed Holocene values this century. Nature. 2020 Oct;586(7827):70–4.

25. Reyes AV, Carlson AE, Beard BL, Hatfield RG, Stoner JS, Winsor K, et al. South Greenland ice-sheet collapse during Marine Isotope Stage 11. Nature. 2014 Jun;510(7506):525–8.

26. de Vernal A, Hillaire-Marcel C. Natural Variability of Greenland Climate, Vegetation, and Ice Volume During the Past Million Years. Science. 2008 Jun 20;320(5883):1622–5.

27. Snyder CW. Evolution of global temperature over the past two million years. Nature. 2016 Oct;538(7624):226–8.

28. Nehrbass-Ahles C, Shin J, Schmitt J, Bereiter B, Joos F, Schilt A, et al. Abrupt CO2 release to the atmosphere under glacial and early interglacial climate conditions. Science. 2020 Aug 21;369(6506):1000–5.

29. Tye GJ, Sherriff J, Candy I, Coxon P, Palmer A, McClymont EL, et al. The δ18O stratigraphy of the Hoxnian lacustrine sequence at Marks Tey, Essex, UK: implications for the climatic structure of MIS 11 in Britain. Journal of Quaternary Science. 2016;31(2):75–92.

30. Koutsodendris A, Pross J, Müller UC, Brauer A, Fletcher WJ, Kühl N, et al. A short-term climate oscillation during the Holsteinian interglacial (MIS 11c): An analogy to the 8.2ka climatic event? Global and Planetary Change. 2012 Jul 1;92–93:224–35.

31. Kandiano ES, van der Meer MTJ, Schouten S, Fahl K, Sinninghe Damsté JS, Bauch HA. Response of the North Atlantic surface and intermediate ocean structure to climate warming of MIS 11. Sci Rep. 2017 Apr 10;7(1):46192.

32. Irvalı N, Galaasen EV, Ninnemann US, Rosenthal Y, Born A, Kleiven H (Kikki) F. A low climate threshold for south Greenland Ice Sheet demise during the Late Pleistocene. Proceedings of the National Academy of Sciences. 2020 Jan 7;117(1):190–5.

33. Barker S, Knorr G, Conn S, Lordsmith S, Newman D, Thornalley D. Early Interglacial Legacy of Deglacial Climate Instability. Paleoceanography and Paleoclimatology. 2019;34(8):1455–75.

34. Candy I, Tye G, Coxon P, Hardiman M, Matthews I, Palmer A. A tephra-based correlation of marine and terrestrial records of MIS 11c from Britain and the North Atlantic. Journal of Quaternary Science. 2021;36(7):1149–61.

35. Candy I, Oliveira D, Parkes D, Sherriff J, Thornalley D. Marine Isotope Stage 11c in Europe: Recent advances in marine–terrestrial correlations and their implications for interglacial stratigraphy – a review. Boreas [Internet]. 2024 [cited 2024 Jul 1];n/a(n/a). Available from: https://onlinelibrary.wiley.com/doi/abs/10.1111/bor.12656

36. Irvalı N, Galaasen EV, Ninnemann US, Rosenthal Y, Born A, Kleiven H (Kikki) F. A low climate threshold for south Greenland Ice Sheet demise during the Late Pleistocene. Proceedings of the National Academy of Sciences. 2020 Jan 7;117(1):190–5.

37. Ritz SP, Stocker TF, Grimalt JO, Menviel L, Timmermann A. Estimated strength of the Atlantic overturning circulation during the last deglaciation. Nature Geosci. 2013 Mar;6(3):208–12.

38. Caesar L, Rahmstorf S, Robinson A, Feulner G, Saba V. Observed fingerprint of a weakening Atlantic Ocean overturning circulation. Nature. 2018 Apr;556(7700):191–6.

39. Poli MS, Meyers PA, Thunell RC, Capodivacca M. Glacial-interglacial variations in sediment organic carbon accumulation and benthic foraminiferal assemblages on the Bermuda Rise (ODP Site 1063) during MIS 13 to 10. Paleoceanography [Internet]. 2012 Sep 1 [cited 2023 Sep 27];27(3). Available from: https://agupubs.onlinelibrary.wiley.com/doi/10.1029/2012PA002314

40. Galaasen EV, Ninnemann US, Kessler A, Irvalı N, Rosenthal Y, Tjiputra J, et al. Interglacial instability of North Atlantic Deep Water ventilation. Science. 2020 Mar 27;367(6485):1485–9.

41. Moffa-Sanchez P, Hall IR, Thornalley DJR, Barker S, Stewart C. Changes in the strength of the Nordic Seas Overflows over the past 3000 years. Quaternary Science Reviews. 2015 Sep 1;123:134–43.

42. Köhl A. Variable source regions of Denmark Strait and Faroe Bank Channel overflow waters. Tellus A: Dynamic Meteorology and Oceanography. 2010 Jan;62(4):551–68.

43. Doherty JM, Ling YF, Not C, Erler D, Bauch HA, Paytan A, et al. Freshening, stratification and deep-water formation in the Nordic Seas during marine isotope stage 11. Quaternary Science Reviews. 2021 Nov 15;272:107231.

44. Kandiano ES, Bauch HA, Fahl K, Helmke JP, Röhl U, Pérez-Folgado M, et al. The meridional temperature gradient in the eastern North Atlantic during MIS 11 and its link to the ocean–atmosphere system. Palaeogeography, Palaeoclimatology, Palaeoecology. 2012 May 15;333–334:24–39.

45. Gregoire LJ, Ivanovic RF, Maycock AC, Valdes PJ, Stevenson S. Holocene lowering of the Laurentide ice sheet affects North Atlantic gyre circulation and climate. Clim Dyn. 2018 Nov 1;51(9):3797–813.

46. Blaschek M, Renssen H, Kissel C, Thornalley D. Holocene North Atlantic Overturning in an atmosphere-ocean-sea ice model compared to proxy-based reconstructions. Paleoceanography. 2015;30(11):1503–24.

47. Sgubin G, Swingedouw D, Drijfhout S, Mary Y, Bennabi A. Abrupt cooling over the North Atlantic in modern climate models. Nat Commun. 2017 Feb 15;8(1):14375.

48. Wouters B, Sasgen I. Increasing Freshwater Fluxes from the Greenland Ice Sheet Observed from Space. Oceanography. 2022 Jul 14;35(3–4):103–5.

49. Thornalley DJR, Oppo DW, Ortega P, Robson JI, Brierley CM, Davis R, et al. Anomalously weak Labrador Sea convection and Atlantic overturning during the past 150 years. Nature. 2018 Apr;556(7700):227–30.

50. Curtis PE, Fedorov AV. Collapse and slow recovery of the Atlantic Meridional Overturning Circulation (AMOC) under abrupt greenhouse gas forcing. Clim Dyn [Internet]. 2024 Apr 6 [cited 2024 Apr 8]; Available from: https://doi.org/10.1007/s00382-024-07185-3

51. Thornalley DJR, Blaschek M, Davies FJ, Praetorius S, Oppo DW, McManus JF, et al. Long-term variations in Iceland–Scotland overflow strength during the Holocene. Climate of the Past. 2013 Sep 3;9(5):2073–84.

52. Koman G, Bower AS, Holliday NP, Furey HH, Fu Y, Biló TC. Observed decrease in Deep Western Boundary Current transport in subpolar North Atlantic. Nat Geosci. 2024 Oct 4;1–6.

53. Collins M, Knutti R, Arblaster J, Dufresne JL, Fichefet T, Friedlingstein P, et al. Long-term Climate Change: Projections, Commitments and Irreversibility. In: Climate Change 2013 - The Physical Science Basis: Contribution of Working Group I to the Fifth Assessment Report of the Intergovernmental Panel on Climate Change [Internet]. Cambridge University Press; 2013 [cited 2024 Aug 2]. p. 1029–136. Available from: https://research.monash.edu/en/publications/long-term-climate-change-projections-commitments-and-irreversibil

54. Shimada C, Sato T, Toyoshima S, Yamasaki M, Tanimura Y. Paleoecological significance of laminated diatomaceous oozes during the middle-to-late Pleistocene, North Atlantic Ocean (IODP Site U1304). Marine Micropaleontology. 2008 Oct 1;69(2):139–50.

55. Hansen B, Østerhus S. North Atlantic–Nordic Seas exchanges. Progress in Oceanography. 2000 Feb 1;45(2):109–208.

56. McCave IN, Thornalley DJR, Hall IR. Relation of sortable silt grain-size to deep-sea current speeds: Calibration of the ‘Mud Current Meter.’ Deep Sea Research Part I: Oceanographic Research Papers. 2017 Sep 1;127:1–12.

57. Rahmstorf S, Box JE, Feulner G, Mann ME, Robinson A, Rutherford S, et al. Exceptional twentieth-century slowdown in Atlantic Ocean overturning circulation. Nature Clim Change. 2015 May;5(5):475–80.

58. Telford RJ, Li C, Kucera M. Mismatch between the depth habitat of planktonic foraminifera and the calibration depth of SST transfer functions may bias reconstructions. Climate of the Past. 2013 Mar 22;9(2):859–70.

59. Moffa-Sánchez P, Moreno-Chamarro E, Reynolds DJ, Ortega P, Cunningham L, Swingedouw D, et al. Variability in the Northern North Atlantic and Arctic Oceans Across the Last Two Millennia: A Review. Paleoceanography and Paleoclimatology. 2019;34(8):1399–436.

60. Muir LC, Fedorov AV. Evidence of the AMOC interdecadal mode related to westward propagation of temperature anomalies in CMIP5 models. Clim Dyn. 2017 Mar 1;48(5):1517–35.

61. Wharton J. Thermal structure of the Northwest Atlantic during the last 25,000 years [Internet] [PhD Thesis]. UCL (University College London); 2023 [cited 2023 Dec 21]. Available from: https://discovery.ucl.ac.uk/id/eprint/10164435/

62. Keil P, Mauritsen T, Jungclaus J, Hedemann C, Olonscheck D, Ghosh R. Multiple drivers of the North Atlantic warming hole. Nat Clim Chang. 2020 Jul;10(7):667–71.

63. Gil IM, Keigwin LD, Abrantes F. The deglaciation over Laurentian Fan: History of diatoms, IRD, ice and fresh water. Quaternary Science Reviews. 2015 Dec 1;129:57–67.

64. Hawkings JR, Wadham JL, Benning LG, Hendry KR, Tranter M, Tedstone A, et al. Ice sheets as a missing source of silica to the polar oceans. Nat Commun. 2017 Jan 25;8(1):14198.

65. Hendry KR, Huvenne VAI, Robinson LF, Annett A, Badger M, Jacobel AW, et al. The biogeochemical impact of glacial meltwater from Southwest Greenland. Progress in Oceanography. 2019 Sep 1;176:102126.

66. Voelker AHL, Rodrigues T, Billups K, Oppo D, McManus J, Stein R, et al. Variations in mid-latitude North Atlantic surface water properties during the mid-Brunhes (MIS 9–14) and their implications for the thermohaline circulation. Climate of the Past. 2010 Aug 27;6(4):531–52.

67. Oppo DW, Lehman SJ. Mid-Depth Circulation of the Subpolar North Atlantic During the Last Glacial Maximum. Science. 1993 Feb 19;259(5098):1148–52.

68. Xuan C, Channell JET, Hodell DA. Quaternary magnetic and oxygen isotope stratigraphy in diatom-rich sediments of the southern Gardar Drift (IODP Site U1304, North Atlantic). Quaternary Science Reviews. 2016 Jun 15;142:74–89.

69. Gottschalk J, Vázquez Riveiros N, Waelbroeck C, Skinner LC, Michel E, Duplessy JC, et al. Carbon isotope offsets between benthic foraminifer species of the genus Cibicides (Cibicidoides) in the glacial sub-Antarctic Atlantic. Paleoceanography. 2016;31(12):1583–602.

70. Hodell DA, Kanfoush SL, Venz KA, Charles CD, Sierro FJ. The Mid-Brunhes Transition in Odp Sites 1089 and 1090 (Subantarctic South Atlantic). In: Earth's Climate and Orbital Eccentricity: The Marine Isotope Stage 11 Question [Internet]. American Geophysical Union (AGU); 2003 [cited 2023 Sep 25]. p. 113–29. Available from: https://onlinelibrary.wiley.com/doi/abs/10.1029/137GM09

71. McManus JF, Oppo DW, Cullen JL. A 0.5-Million-Year Record of Millennial-Scale Climate Variability in the North Atlantic. Science. 1999 Feb 12;283(5404):971–5.

72. Laskar J, Robutel P, Joutel F, Gastineau M, Correia ACM, Levrard B. A long-term numerical solution for the insolation quantities of the Earth. A&A. 2004 Dec 1;428(1):261–85.

73. Hall IR, Becker J. Deep Western Boundary Current variability in the subtropical northwest Atlantic Ocean during marine isotope stages 12–10. Geochemistry, Geophysics, Geosystems [Internet]. 2007 [cited 2023 Sep 26];8(6). Available from: https://onlinelibrary.wiley.com/doi/abs/10.1029/2006GC001518

74. Giosan L, Flood RD, Grützner J, Franz SO, Poli MS, Hagen S. High-resolution carbonate content estimated from diffuse spectral reflectance for Leg 172 sites. In: In Keigwin, LD, Rio, D, Acton, GD, and Arnold, E(Eds), Proc ODP, Sci Results [Internet]. 2001 [cited 2023 Dec 29]. p. 1–12. Available from: https://epic.awi.de/id/eprint/20958/1/Gio2001b.pdf

75. Parker RL, Foster GL, Gutjahr M, Wilson PA, Obrochta SP, Fagel N, et al. The history of ice-sheet retreat on North America during Termination 5: Implications for the origin of the sea-level highstand during interglacial stage 11. Earth and Planetary Science Letters. 2023 Sep 15;618:118286.

76. Kandiano ES, van der Meer MTJ, Bauch HA, Helmke J, Damsté JSS, Schouten S. A cold and fresh ocean surface in the Nordic Seas during MIS 11: Significance for the future ocean. Geophysical Research Letters. 2016;43(20):10,929-10,937.

77. Melles M, Brigham-Grette J, Minyuk PS, Nowaczyk NR, Wennrich V, DeConto RM, et al. 2.8 Million Years of Arctic Climate Change from Lake El'gygytgyn, NE Russia. Science. 2012 Jul 20;337(6092):315–20.

78. Hu HM, Marino G, Pérez-Mejías C, Spötl C, Yokoyama Y, Yu J, et al. Sustained North Atlantic warming drove anomalously intense MIS 11c interglacial. Nat Commun. 2024 Jul 15;15(1):5933.

79. Zhao X, Cheng H, Sinha A, Zhang H, Baker JL, Chen S, et al. A High-Resolution Speleothem Record of Marine Isotope Stage 11 as a Natural Analog to Holocene Asian Summer Monsoon Variations. Geophysical Research Letters. 2019;46(16):9949–57.

80. Hodell D, Crowhurst S, Skinner L, Tzedakis PC, Margari V, Channell JET, et al. Response of Iberian Margin sediments to orbital and suborbital forcing over the past 420 ka. Paleoceanography. 2013;28(1):185–99.

81. Bouchet M, Landais A, Grisart A, Parrenin F, Prié F, Jacob R, et al. The Antarctic Ice Core Chronology 2023 (AICC2023) chronological framework and associated timescale for the European Project for Ice Coring in Antarctica (EPICA) Dome C ice core. Climate of the Past. 2023 Nov 10;19(11):2257–86.

Acknowledgments:

We thank staff at the IODP repository, Bremen, for core sampling. We also thank Nil Irvali (University of Bergen) for data comparison for U1305. We thank technical staff at University College London (Eileen Cheng, James Shilland, Bonnie Atkinson, Ian Patmore, Eirini Papadopopolous) and Royal Holloway, University of London (Marta Perez Fernandez). We thank James Channell for Relative PalaeoIntensity datasets. We thank James Rolfe (Godwin Laboratory) for isotopic analysis of foraminifera. Chat GPT was used to edit issues with coding for data presentation.

Funding:

NERC grant London DTP840 (NE/S007229/1) – DP.

NERC Project ReconAMOC (NE/S009736/1) – DT.

NERC Project VARING: NE/V001620/1 – DT.

European Union's Horizon Europe Project 101059547 – EPOC – DT.

Angelina Messina TMS grant – DP.

Author contributions:

Conceptualization: DP, IC, DT, EM, I.M, A.P.

Methodology: DP, IC, DT, AP.

Investigation: DP, IC, DT, EM, DF, MC, SN, IM, AP.

Visualization: DP, IC, DT, JW.

Funding acquisition: DP, IC, DT.

Project administration: DP, IC, DT, EM.

Supervision: IC, DT, EM, AP, IM.

Writing – original draft: DP, IC, DT.

Writing – review & editing: DP, IC, DT, JW, EM, AP.

Competing interests: Authors declare that they have no competing interests.

Data and materials availability: Data is available on request and will be made available on PANGEA upon publication (**insert link when available**)

Main text figure captions:

Fig. 1. Core locations and data synthesis compared to key climate forcings: (Top) IODP Site U1302 (50.2°N, 45.6°W; 3250m depth) (this study); IODP Site U1305 (57.5°N, 48.5°W; 3463m depth) (this study, (36); ODP Site 983 (60.4°N, 23.6°W; 1983m depth) (this study, (33); ODP Site 984 (61.0°N, 24.0°W; 1650m depth) (this study); IODP Site U1304 (53.1°N, 33.5°W; 3024m depth) (this study); ODP Site 980 (55.5°N, 14.7°W; 2170m depth) (this study, (71); projected on a map of North Atlantic Sea Surface Temperatures (200m depth) using data from

WOA18 plotted using Ocean Data View. Study core sites are depicted as white circles with black outlines. Key comparison sites in this study are depicted by black circles. Key surface (solid) and intermediate/deep (dashed) ocean currents are depicted. (**A, C**) Key climate forcings (duplicated above each dataset) including greenhouse gas data (CO_2 and CH_4) from EPICA Dome C (28) and summer insolation data at July 65°N (72). (**B**) % *Neogloboquadrina pachyderma* records compared with compiled normalised Ice Rafted Debris records from study sites. (**D**) Mean sortable silt data compared with a compiled normalised Ice Rafted Debris record from study sites. Coloured bars: grey at onset and end of MIS 11c = ice rafting intervals; light grey = broad mid-interglacial cooling; dark grey = abrupt mid-interglacial cooling.

Fig. 2. Compiled Nordic Seas overflow records compared to the AMOC index and potential forcing mechanisms during the main interglacial period of MIS 11c: (**A**) Reconstructed AMOC index ($AMOC_{SPG-T}$) presented as (red) global sea surface temperature anomaly with reference to modern and (black) percent change with reference to modern AMOC (~ 18 Sv) (see Methods for more details). (**B**) Combined Nordic Seas overflow record ($AMOC_{NSO}$) across MIS 11c presented as percent change with reference to modern, assuming an equal contribution of both DSOW and ISOW. ISOW is depicted as a purple dashed line. DSOW is depicted as a green dotted line. Error bars shown for AMO_{NSO} (1σ and 2σ) were generated using a Monte-carlo runs with a 1 cm s^{-1} error attributed, in addition to random perturbations using age tie point uncertainties from this study (see SI) (**C**) Proxy records (Benthic $d^{13}C$ and % $CaCO_3$) of changes in the Deep Western Boundary Current (DWBC) from ODP Site 1063 (39,73). % $CaCO_3$ was calculated using equations from (74). (**D**) Record Sea surface temperature indicator (% *N.pachyderma*) record from the northern Subpolar Gyre (IODP Site U1305), highlighting the saturation of % *N.pachyderma* at 417 ka, earlier than other sites (see Fig. 1B), suggesting sea ice formation and reduction in local convective activity. (**E**) Greenland ice sheet dynamics derived from $CaCO_3$-free silt flux (grey dotted polygon) (25) and pollen concentrations (green polygon) (26). Modelled GrIS meltwater flux was derived from Robinson et al. (2017) (see SI) (grey solid line) and has been temporally adjusted within age model uncertainties so that the highest rates of meltwater flux coincide with the smallest sGrIS extent. Note this has been inverted. Coloured bars: light grey = broad mid-interglacial cooling; dark grey = abrupt mid-interglacial cooling.

Fig. 3. Records of Nordic Seas overflows compared to key forcings across MIS 11c: (75). (**A-D**) Compiled ISOW record compared to forcing mechanisms. **(A):** Boreal summer insolation was obtained from (72). **(B):** Compiled ISOW record (purple) derived from Sites 983 and 984 **(C):** Oxygen isotopes derived from planktic foraminifera *N.pachyderma* (black) and *T.quinqueloba* (grey) (76). Highlighted in red are consistent (multi-datapoint) offsets of ≥0.4‰, indicating a thermal regime, favouring increased convection and stronger ISOW. **(D):** Nitrate utilisation (^{15}N) indicates reduced utilisation during the mid-late interglacial, indicating increased mixed-layer depth, favouring convection (43); (**E-H**) Compiled DSOW record compared to forcing mechanisms. **(E):** Boreal summer insolation was derived from (72). **(F):** Compiled DSOW record from Sites U1302 and U1305 (green); **(G-H):** Lead isotope data indicates the earliest **(G)** and latest **(H)** timing of the Laurentide Ice Sheet retreating to the late Holocene extent (Canadian Archipelago) on the age model of this study (late Holocene levels = dashed line). The larger Laurentide Ice Sheet coincides with strongest DSOW. All records are presented relative to their modern values (WOCE SSTs and modern coretop mean sortable silt values). Error bars shown for DSOW and ISOW (1σ and 2σ) were generated using a Monte-carlo runs with a 1 cm s^{-1} error attributed, in addition to random perturbations using age tie point uncertainties from this study (see SI). Coloured bars: light blue = broad mid-interglacial AMOC weakening; dark blue = abrupt mid-interglacial AMOC weakening.

Fig. 4. Global comparison of key MIS 11c records that show evidence for mid-interglacial instability associated with AMOC weakening: (**A**) Temperature and key vegetational data from Marks Tey palaeolake, Northwestern Europe. Oxygen isotope data from authigenic calcite laminations indicating changes in summer air temperature (29). Solid black line = 11.pt running mean; translucent grey line = raw data. Error is 1σ = 0.09; compared with percentage change in grass pollen (29), with increasing percentages indicating an open landscape (note reversed axis). Data from Marks Tey has been aligned to the study age model using the age of the tephra layer at ODP Site 980 (34). Note that Marks Tey data is presented on depth as just the varved section (~ 12 – 16) has robust chronological control, whilst the rest of the sequence does not have a known sedimentation rate. **(B)**: Pollen-based temperature (red) and precipitation (blue) reconstructions from North-east Siberia (77). WMT = Warmest month temperature; MAP = Mean annual precipitation. Error bars show highest and lowest values. (**C**) Strontium Calcium ratios from Bàsuru Cave speleothem record, Northern Italy (78). Higher values (note reversed axis) indicate cooler, drier conditions. (**D**) Oxygen isotope data from Yongxing Cave speleothem record from Eastern China. Higher values (note reversed axis) indicate weaker Asian Summer Monsoon (79). Blue lines for both B and C are the suggested equivalent of the mid-MIS 11c severe AMOC weakening and have been highlighted due to the high variability in these records (**E**) Alkenone ($U^{k}_{37'}$) derived Sea Surface Temperature record of MIS 11c from Site MD01-2443 (37.9^{o}N, 10.2^{o}W; water depth 2925m), Iberian margin, on the age model of this study (44). (**F**) Faunal (Modern Analogue Technique) Sea Surface Temperature record of MIS 11c from ODP Site 958 (24.0^{o}N, 20.0^{o}W; water depth 3728m), North-west African margin, on the age model of this study (80). (**G**) $AMOC_{SPG-T}$ presented as a comparison to global records of MIS 11c. (**H**) Global climate forcings including Carbon dioxide (red), methane (green) (28) and insolation (dashed black) (72). Light blue shading indicates broad AMOC weakening, dark blue shading indicates abrupt AMOC weakening. Dashed blue line from top to bottom indicates the potential equivalent stratigraphic positions of the onset of AMOC weakening at ~ 417 ka in this study, marked by the CDJ- event in panel F. Note that the greenhouse gas concentrations are on AICC2023 (81), as is the data from this study.

Title: Weakening of AMOC linked to past Greenland Ice Sheet retreat

SUPPLEMENTARY INFORMATION

Authors: D. Parkes[1,2]*†, D. Thornalley[2]†, E. McClymont[3]‡, S. Nuber[2]§¶, D. Fairman[2], M. Cousins[2]§, A. Palmer[1]‡, I.P. Matthews [1]‡, J. Wharton[2] I. Candy[1]†.

Affiliations:

[1]Department of Geography, Royal Holloway, University of London; Egham, TW20 0EX, United Kingdom.

[2]Department of Geography, University College London; London, WC1E 6BT, United Kingdom.

[3]Department of Geography, University of Durham; Durham, DH1 3LE, United Kingdom.

*ucfadre@ucl.ac.uk

†These authors are the primary investigators of this work.

‡These authors assisted in the conception and co-supervision of this work.

§These authors contributed towards data collected in this work.

¶This author is now at University of Washington, U.S.

Materials and Methods:

Study site selection:

In the Labrador Sea, IODP Sites U1302 (50.2ºN, 45.6ºW; 3250m depth) and U1305 (57.5ºN, 48.5ºW; 3463m depth) are ideally situated to monitor changes in subpolar climate proximal to Greenland. South of Iceland, ODP Sites 983 (60.4ºN, 23.6ºW; 1983m depth) and 984 (61.0ºN, 24.0ºW; 1650m depth) monitor changes in the Polar Front (PF) (1). Site U1304 (53.1ºN, 33.5ºW; 3024m depth) monitor changes in the Sub-Arctic Convergence (SAC) (2). Site 980 (55.5ºN, 14.7ºW; 2170m depth) contains the tephra layer which links SST changes to annually laminated lake sediments in Britain (3). Together, these monitor the Sub-Polar Gyre (SPG), the most sensitive region to AMOC weakening (4). Furthermore, Sites 983 and 984 monitor the production of Iceland Scotland Overflow Water (ISOW), whilst Sites U1305 and U1302 monitor the production of Denmark Strait Overflow Water (DSOW). Combined, these form the densest component of North Atlantic Deep Water (Lower NADW) constituting approximately two-thirds of overall NADW production (5). The remaining third is Upper NADW, formed in the open subpolar North Atlantic, also termed Labrador Seawater (LSW).

Sediment washing and preparation for faunal and sortable silt analysis:

Sediment samples for all sites were ordered from the IODP repository, Bremen, ready for processing at UCL Geography Laboratory. These were weighed upon arrival, frozen, freeze-dried, and weighed again. Dried samples were gently disaggregated on a rotating wheel overnight before being wet sieved through a 63µm sieve with deionized water. The <63µm fraction underwent the $\overline{SS}$ process. Coarse samples were dried at < 40ºC before weighing and collecting in 5ml vials ready for foram-census and Ice-Rafted Debris counts using a low-powered Leica stereo microscope.

Sortable silt preparation and analysis:

The < 63μm fraction was left until settled after washing. After settling, water was siphoned off and the slurry of sediment was transferred to conical flasks using 2M acetic acid. Samples were topped up to 150ml of acetic acid and gently swirled. Sediment was then left to settle until at least the next day. Once settled, samples were siphoned again before adding another 100 – 150ml of acetic acid, then swirled to mix well. Samples were left to settle again until at least the next day. Once settled, the acetic acid was siphoned off before filling with De-Ionized (DI) water. Samples were again left to settle until at least the next day. Once settled, 200ml of 2M sodium carbonate was added to each sample whilst swirling. Flasks were placed in a water bath that had been set to 85ºC for at least 5 hours, stirring at 2 and 4 hours. Once removed, samples were given time to cool and settle before siphoning off sodium carbonate and adding DI water. This process removes silicates and opal. Samples were left to settle at least until the next day. Once settled, samples were siphoned before adding another fill of DI to rinse. Samples were then left to settle for several days. Once settled, samples were siphoned to remove DI before transferring into Nalgene bottles using 0.2% Calgon. At this point samples were ready for analysis. Sortable silt values were measured using a Beckman Coulter Multi-Sizer 4. Samples were placed for 24 hours on a rotating wheel, and then ultra-sonicated for 3 minutes to disaggregate particles. Samples were well shaken for 10 seconds with the lid on before removing the lid and shaking for a further 10 seconds. Aliquots were pipetted into the Beckman Coulter Multi-Sizer 4 glass beaker, that has a nipple in the base to induce turbulent flow in the fluid. At least 2 aliquots were used per measurement to reduce pipetting errors. Particles were suspended in an electrolyte and drawn through a small aperture where they displace their volume of electrolyte causing impedance changes, which are sized and counted with a total 70,000 particles counted per run. Samples were run at least twice; however, further measurements were taken if repeat runs were not within less than 0.8μm of each other. All runs were averaged to provide a measure of mean Sortable Silt. The Sortable Silt mean size was calculated in the normal sedimentological convention on log-transformed weight (or volume) frequency size of the 10–63 μm range. ODP 980 was not selected for sortable silt analysis due to: (i) the presence of a re-circulating gyre in Rockall Trough; and (ii) ISOW is not the major control on flow speed at this location.

$AMOC_{NSO}$ Reconstruction

The Nordic Seas overflows directly provide ~ 30% of the volume transport of the lower limb of the AMOC (5). By the time these overflows reach the study sites they have undergone entrainment and doubled their volume to make up ~ 2/3 of AMOC strength. Consequently, reconstructing changes in the strength of the Nordic Seas overflows at the study sites provides a physical measure of a key AMOC component. This study reconstructs both components of the Nordic Seas overflows, ISOW and DSOW. To examine changes in the overall strength of Nordic Seas overflows, the individual mean sortable silt records for ISOW (Sites 983 and 984) and DSOW (Sites U1302 and U1305) were converted into flowspeeds. Once converted from mean sortable silt to flowspeed (Equation 1), each site record was linearly interpolated onto a common time step (every 300 years between 400 and 425 ka) and averaged to create records of ISOW and DSOW. To generate an overall record of changes in Nordic Seas overflow strength, the ISOW and DSOW records were converted into percentage change with reference to modern coretop flowspeeds, then the total strength of the overflow was calculated by taking the average of the changes in each overflow relative to modern and MIS 11c.

Flowspeeds were calculated using the Equation 1, which is derived from, and only marginally differs from the 'Main Line' calibration of McCave *et al*. (2017) (Equation 2), with the minor modification due to slightly different values obtained when running calibration samples at UCL.

Equation 1. Calculating flow speed (from Coulter Counter data)*. U = Velocity (flow speed) in cm/s and* $\overline{SS}$ *= mean sortable silt grain size in mm.*

$$U = 1.205 \times \overline{SS} - 20.12$$

Equation 2. Original flow speed calculation (for Coulter Counter data)*. U = Velocity (flow speed) in cm/s and* $\overline{SS}$ *= mean sortable silt grain size in mm (McCave et al., 2017).*

$$U = 1.23 \times \overline{SS} - 19.53$$

$AMOC_{NSO}$ errors were generated by running a series of Monte-Carlo simulations for individual site records and propagating the errors to get a combined overflow error. A flowspeed error of 1 cm s^{-1} was attributed (McCave and Andrews, 2017), in addition to random perturbations using age tie point uncertainties from this study in order to incorporate both measured proxy and age model uncertainties.

$AMOC_{SPG-T}$ Reconstruction

Changes in the surface ocean temperature of the SPG region has been suggested to be a proxy for AMOC strength (4). This is based on a weakening AMOC reducing the advection of heat to this region, such that the difference between the average of the surface ocean temperature anomaly in SPG region and the global SST anomaly provides an estimate of AMOC strength (Fig 4.5) (4,7). Caesar *et al* (2018) used November to May SST anomalies, which is compatible with our use of planktic foraminiferal faunal 'SSTs' since these likely reflect temperatures at ~ 75m depth (8), which are mainly set during the deeper mixing of winter-spring. In Caesar *et al*. (2018), only sites in the central/western SPG region were included in the $AMOC_{SPG-T}$ index; however, other work has shown that sites in the northeast Atlantic may also be sensitive to shifts in the AMOC, and longer timescales (multi-centennial) AMOC changes have been associated with a broader North Atlantic warming pattern (9–12). Consequently, all sites in this study have been included in the SPG index, noting that not all sites contain data for the intervals 425 – 423 ka and 404 – 400 ka (see Appendix 2 for which sites were used for each time interval). The main time interval (423 – 405 ka) for this study includes data from all sites.

There has been criticism of this approach to reconstructing AMOC (13). The "warming hole" in the SPG region has been attributed to AMOC slowdown by some (4), but others suggest this overlooks the multitude of physical mechanisms that control North Atlantic surface ocean temperatures. Over longer timescales, reconstructions of AMOC fingerprint have compared well with proxy reconstructions of ocean circulation and the broader warming of the subpolar North Atlantic during a strong AMOC is consistent with the bipolar seesaw concept (11). Furthermore, we compare our AMOC fingerprint reconstruction to physical records of deep ocean current strength.

For the calculation of the AMOC index, ($AMOC_{SPG-T}$), study site SSTs were generated using a combination of *Nps*-inferred SSTs for records with %*Nps* values typically between 20 and 90 % abundance (Sites U1302 and U1305), and Modern Analogue Technique (MAT)-inferred SSTs for sites where %Nps consistently exceed these values (Sites 980, 983, 984, and U1304). The modern SST values were taken from WOCE datasets (MAT SSTs) and Kucera *et al*. (2005) for *Nps* percentages.

Once individual records of SSTs were generated, each site record was linearly interpolated onto a common time step (every 300 years between 400 and 425 ka), with the exception of Sites 983 and 984 which were combined into a single record due to their proximity. To generate an $AMOC_{SPG-T}$, each SST record was converted into percentage change relative to modern. The interpolated records of each site were then averaged to obtain an average SST anomaly for the subpolar North Atlantic relative to modern. The global temperature anomaly (T) was generated by linearly interpolating the temperature record from Shakun *et al*. (2015), onto the same timestep as the SST records. $AMOC_{SPG-T}$ was then calculated by subtracting the Shakun *et al.* (2015) dataset from the generated combined SST anomaly (see Equation 3). To examine changes in AMOC strength, the $AMOC_{SPG-T}$ values were multiplied by 2.3 following Rahmstorf *et al.* (2015) and compared to modern AMOC strength (~ 18 Sv) by converting into percentage change.

$AMOC_{SPG-T}$ errors were generated by running a series of Monte-Carlo simulations for individual site records and propagating the errors to get a combined SST anomaly error. This was also propagated through the global temperature anomaly error. An SST error of 1°C was attributed, in addition to random perturbations using age tie point uncertainties from this study in order to incorporate both measured proxy and age model uncertainties.

Equation 3: AMOC fingerprint following Caesar et al. (2018): *I_{AMOC} = AMOC fingerprint. $\overline{SST}_{NAtl}$ = mean SST records from ODP Sites 980 (MAT), 983/984 (MAT), IODP Sites U1304 (MAT), U1305 (Nps-SSTs), and U1302 (Nps-SSTs). MAT has been used where % Nps was regularly below 20%. $\overline{SST}_{Global}$ = Global SST Anomaly (Shakun et al., 2015).*

$$I_{AMOC} = \overline{SST}_{SPG} - \overline{SST}_{Global}$$

Isotopic analysis of planktic and benthic foraminifera:

Stable isotope measurements on planktic foraminifera assemblages of *Nps* were targeted at intervals of particularly low resolution in the updated age model, resulting in 34 new samples. 30 specimens per sample (~ 150 – 200μg) were hand-picked from the 150 - 250μm size fraction. These were run at the Godwin Laboratory, University of Cambridge. Foraminifera are transferred into sample vials, crushed, and soaked in a solution of 3% Hydrogen Peroxide for 30 minutes. Acetone (AR) is added and the sample ultrasonicated for 10 seconds and then the liquid is carefully decanted off using a tissue. The samples are dried in an oven at 50ºC overnight. The vials are sealed with a septa and screw cap and the samples are analysed using a Micromass Multicarb Sample Preparation System attached to a VG SIRA Mass Spectrometer. Each run of 30 samples is accompanied by 10 reference carbonates and 2 control samples. The results are reported with reference to the international standard VPDB and the precision is better than +/-0.08‰ for $^{18}O/^{16}O$.

Samples of *Cibicidoides wuellerstorfi* (*C.wull*) (IODP U1304), *Cib.sp* (ODP 984) were run at the Godwin Laboratory, Cambridge. Foraminifera are transferred to sample vials, crushed and then dried in an oven at 50ºC. The vials are loaded on a carousel and analysed using a Thermo Kiel device attached to a Thermo MAT253 Mass Spectrometer in dual inlet mode. The preparation system operates automatically analysing samples in sequence. 104% orthophosphoric acid is dropped onto the evacuated vial and reacts with the Calcium Carbonate sample. The evolved Carbon Dioxide is cryogenically dried and then admitted to the dual inlet mass spectrometer for isotopic analysis by comparison with a reference gas. Each run of 30 samples is accompanied by 10 reference carbonates and 2 control samples. The results are reported with reference to the international standard VPDB and the precision is better than +/-0.08‰ for $^{18}O/^{16}O$.

Supplementary Text

1. Age model construction

A common age model for MIS 11c was produced for study sites in the North Atlantic region. This was done by (1) choosing a tuning target (in this case, GLT_{Syn}); (2) tuning the % *Nps* record of ODP Site 980 to this; (3) tuning the remaining marine sediment core records (ODP Sites 983 and 984, and IODP Sites U1304 and U1305) to Site 980 using stable oxygen isotopes of benthic foraminifera, Relative PalaeoIntensity, and major increases in Ice-Rafted Debris; (4) tuning IODP Site U1302 to Site U1305 through planktic foraminifera stable oxygen isotopes, Relative PalaeoIntensity, and major increases in IRD. Additional stable isotope data were generated to help facilitate this.

Constructing a base age model using GLT_{Syn} as a tuning target

This study utilises the Synthetic Greenland Temperature record (GLT_{Syn}) on the AICC2023 chronology (1,14–16). Changes in Greenland air temperature are thought to correlate with SST changes in the subpolar North East Atlantic (1). GLT_{Syn} is derived from the Antarctic temperature record from Jouzel *et al.* (2007). It is based on the thermal bipolar seesaw millennial-scale relationship between Greenland and Antarctica (14,17). According to this model, we should see an antiphase relationship between the rate of change of Antarctic temperature and the Greenland temperature anomaly. This is complicated by uncertainties associated with ice age-gas age offsets; however, it has reproduced much of the variability seen in the physical Greenland temperature record (14).

Beyond the radiocarbon limit, it is difficult to independently align records due to large age uncertainties associated with absolute dating methods; therefore, an alternative approach is necessary. The mid-points of abrupt transitions, in addition to pronounced peaks and troughs, associated with millennial-scale oscillations such as those observed in the Greenland ice core record provide an ideal tuning target for marine proxy data beyond typical absolute dating methods (18).

The AICC2023 chronology using GLT_{Syn} (derived from the Antarctic ice core record) has been chosen to permit comparisons of sites to atmospheric greenhouse gas changes. This relies on the assumption that *Nps* variability in the tuned record (Site 980) reflects changes in the synthetic Greenland air temperature however, the relationship appears reasonable (SI Fig. 1A). The LR04 age model has not been used in this study as it does not account for

866

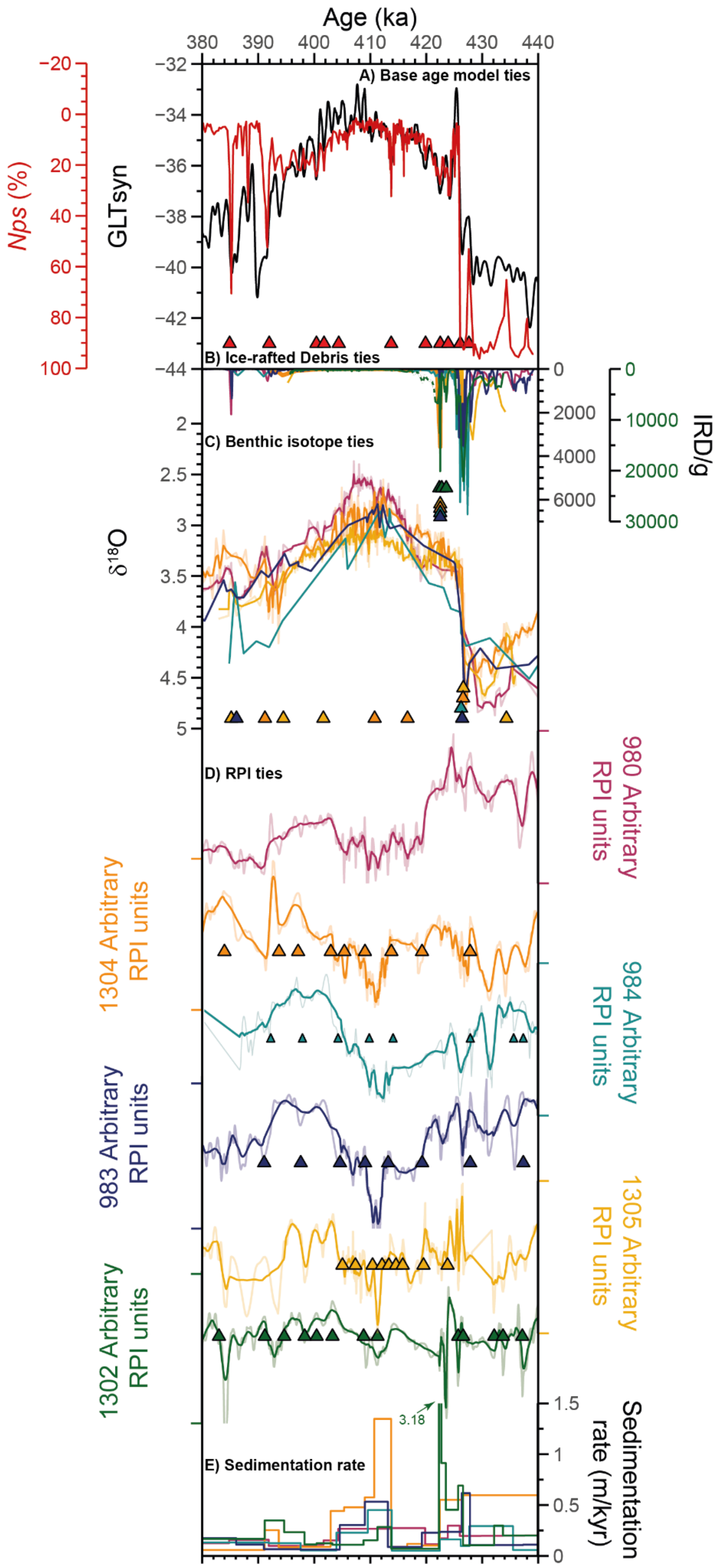
Age (ka)
380 390 400 410 420 430 440
A) Base age model ties
Nps (%)
GLTsyn
B) Ice-rafted Debris ties
IRD/g
C) Benthic isotope ties
$\delta^{18}O$
D) RPI ties
980 Arbitrary RPI units
1304 Arbitrary RPI units
984 Arbitrary RPI units
983 Arbitrary RPI units
1305 Arbitrary RPI units
1302 Arbitrary RPI units
3.18
E) Sedimentation rate
Sedimentation rate (m/kyr)

SI Fig. 1. Study Age model on AICC23: *(**A**) Base age model generated by producing Nps tie points from ODP 980 (red; this study, (60)) (red triangles) to GLT_{syn} (black) on the AICC23 timescale (1,18); (**B**) Ice Rafted debris tie points at 422.5 ka for study sites. (**C**) Benthic oxygen isotope tie points for Sites U1305, U1304, 983, and 984 to ODP 980. U1302 does not presently have a published benthic oxygen isotope record. Sites 980, U1305, and U1304 have mid-weighted 3-point average solid lines with raw data as faded lines of the same colour. (**D**) Relative PalaeoIntensity tie points for Sites U1304, 984, 983, U1305, and U1302, to ODP 980. Sites are placed on a y axis reflecting arbitrary RPI units which have been scaled logarithmically (log(10)). (**E**) Reconstructed sedimentation rates for all study sites on the present age model in metres per kiloyear. Note that the highest sedimentation rate for Site U1302 is beyond the axis limit at 3.18 m/kyr. Coloured triangles indicate tie points to the base age model. These correspond to the colours used for each site. Colours: Red = ODP 980; orange = IODP U1304; yellow = IODP U1305; green = IODP U1302; dark blue = ODP 983; light blue3 = ODP 984.*

changes in sedimentation rate as a result of millennial-scale changes in climate and deep-sea currents, instead assuming a relatively constant sedimentation rate within interglacials (19–21). As this study is conducted across a single interglacial and is primarily focussed with abrupt climate change it would be inappropriate to not account for this.

Following (1,14,18,22), the % *Nps* record of Site 980 has been tuned to mid points, peaks, and troughs of millennial scale oscillations in GLT_{Syn} on AICC2023 (Fig. 1A). Site 980 was chosen for two reasons: (1) Site 980, of all the marine sediment cores used in this study, has the most complete benthic isotope stratigraphy. Consequently, it provides a high-resolution record to tune other sites to; and (2) Site 980 contains a tephra layer during the transition into a cooling event indicated by % *Nps* changes, which is also present at Marks Tey during an interval of isotopic decline (3). It was beyond the scope of this study to look for tephra at all of the marine sites to confidently correlate them, especially because there is no guarantee that this tephra layer would be present at every site, but this would be a useful target for future work. Whilst it is an assumption that we are aligning the same events, it is the best available method for marine sediment cores beyond the radiocarbon limit (18). The following sections will detail how each site was aligned to Site 980 and thus aligned to the AICC2023 timescale.

1.1. Utilising benthic stable oxygen isotope records to tune to Sites to ODP Site 980

Stacks of benthic oxygen isotopes of foraminifera have long been used to correlate sediment cores on glacial-interglacial timescales (20,23–26). This study does not tune each core to the LR04 global benthic oxygen isotope stack for several reasons. The LR04 stack has an age error suggested to be +/- 4 kyr in older interglacials (20,27), which is not suitable for examining the relative timing of millennial-scale events between cores. Whilst GLT_{Syn} on AICC2023 has a similar age uncertainty, GLT_{Syn} contains distinct millennial features, so that the resultant age uncertainties result from the duration of the feature chosen to tune to, which are much smaller. Secondly, the LR04 stack does not account for changes in sedimentation rate at sub-orbital timescales, which is likely to be the case during abrupt climate change events. Thirdly, tuning records directly to Site 980 (on GLT_{Syn}) tunes the records to the Antarctic Ice Core chronology, which is associated with a better precision error than LR04 (28) and allows direct comparison to records of global greenhouse gas changes.

This study does use benthic oxygen isotopic change as tie points during the Terminations and glacial inceptions, as these large magnitude features are likely to be concurrent across all sites due to their relatively close geographic locations. For sub-orbital features, we primarily make use of Relative PalaeoIntensity (RPI).

1.2. Utilising Relative PalaeoIntensity records to tune to Sites to ODP Site 980

RPI is a measure of the strength of the Earth's magnetic field, which was first measured by Gauss in 1835. Consequently, fluctuations should record global scale changes at each site. This can be measured continuously across sediment cores, providing high-resolution records for correlation. A number of PalaeoIntensity stacks *e.g.* PISO-1500 (29); Sint-800 (30); Sint-2000 (31); NAPIS-75 (32) have been generated across a variety of timescales and spatial extents.

The RPI proxy can be generated in a number of ways but usually uses the Natural Remanence Magnetization (NRM) of sediment. This takes into account magnetic field strength, magnetic concentration, lithology, and environmental changes. For RPI to work, it is necessary to remove the lithological component and ideally have a record solely of magnetic field strength. To remove the lithological component, NRM is normalised using one of: Isothermal Remanent Magnetization (IRM), Anhysteretic Remanent Magnetization (ARM), and Susceptibility (33–36). Susceptibility is not commonly used as it is sensitive to large multidomain magnetite grains, often part of IRD, as well as small grains (37). In ideal conditions, each normaliser will produce the same record.

There are several caveats when using RPI to tune sediment records to each other. The first is which normaliser to use, as previously mentioned. Of critical importance, one must also consider the difference in age between particles settling through the water column and when it is locked into position in the sediment (the 'Lock-In Depth'). This has been difficult to quantify; however, any age error associated with this will decrease with higher sedimentation rates (38,39). As such, it is preferable to work with sedimentation rates >6cm/kyr, to record millennial-scale changes in RPI and avoid considerable errors due to Lock-In Depth of magnetised particles. All sites in this study have average sedimentation rates higher than this.

As with benthic isotope work, we have chosen not to tune our record to a specific global or broader regional stack. Instead, we choose to tune our records to Site 980 on for the reasons detailed previously.

1.3. Utilising planktic oxygen isotope records for age model tuning

For most of the sites used in this study, benthic oxygen isotopes from foraminifera and RPI measurements were sufficient to construct a common chronology. For Site U1302 there is a lack of published benthic isotope data due to poor benthic foraminifera preservation and/or abundance at this location; however, there is a detailed planktic isotope record of *Nps* (40). The comparison between surface planktic isotopes of *Nps* at Site U1302 (40) and Site U1305 (41) reveals a striking resemblance between the two throughout the MIS 11c. Consequently, once Site U1305 had been tied to Site 980, Site U1302 was tied to Site U1305 using a combination of RPI and planktic isotopes. It became apparent that the record for Site U1302's much lower temporal resolution (Site U1302 = 111, U1305 = 374 for the MIS 11 interval) prohibited a complete set of robust age model tie points. As a result, 34 further isotope data points were generated during intervals of particularly low resolution.

Nps is common during MIS 11c at Site U1302, allowing for consistent measurements across samples. This species can inhabit a large range of depths; however, it normally occurs in the mesopelagic layer below the pycnocline (42–44). Whilst it is true that planktic isotope records, particularly at high latitudes, can be strongly influenced by ice-surges, meltwater events, and brine rejection (45), the surface water mass in the Labrador sea appears to be broadly consistent across both sites. Furthermore, the use of RPI to improve stratigraphic correlation helps overcome this issue (46).

1.4. Age model presentation and discussion of age uncertainty

The tuning tie points are shown for each site, in addition to the resultant sedimentation rates (Site 980 – SI Fig 2; Site 983 – SI Fig 3; Site 984 – SI Fig 4; Site U1304 – SI Fig 5; Site U1305 – SI Fig 6; Site U1302 - SI Fig 7). Estimation of the relative age uncertainty associated with the tuning tie points was based on the duration of the feature used as a tuning target (*e.g.,* the timespan of a climate transition or a pronounced peak) with the total event duration deemed to be approximately equivalent to $\pm 2\sigma$ (47). Age uncertainties were first calculated for Site 980, which is based on tuning to GLT_{Syn} on AICC2023. Age estimates for the other cores were then calculated by combining the age uncertainty associated with the selection of the tuning target in the chosen core with the (linearly interpolated) Site 980 age uncertainty for the equivalent feature. This age uncertainty estimates the relative error assuming the records have been tuned correctly. To then calculate the uncertainty in the absolute age, these tuning age uncertainties are combined with the published AICC2023 age uncertainties (15).

Tie points and age uncertainties (tuning based, and absolute) are summarised for each study site in SI Tables 1-3. The 2σ age uncertainty for Site 980 ranges from ± 0.10 – 0.59 kyr. The propagated age uncertainty for the remaining sites ranges from: ± 0.07 – 0.52 kyr (Site 983); ± 0.09 – 0.29 kyr (Site 984); ± 0.07 – 0.29 kyr (Site U1304); ± 0.06 – 0.31 kyr (Site U1305); and ± 0.08 – 0.31 kyr (Site U1302). Average 2σ age uncertainties for 380 – 440 ka for each site are: ± 0.24 kyr (Site 980); ± 0.36 kyr (Site 983); ± 0.36 kyr (Site 984); ± 0.32 kyr (Site U1304); ± 0.28 kyr (Site U1305); ± 0.38 kyr (Site U1302). Assuming these have been tuned correctly, these are all sufficient to make assessments about millennial-scale changes in climate as is the focus of this study. Absolute age uncertainties are much larger (2σ of 2 – 5 kyr), dominated by the age uncertainty in the AICC2023 chronology. These much larger absolute age uncertainty estimates are relevant when comparing the results from this study to records that have age-scales that have been constructed independent of the AICC2023 chronology but are not relevant when comparing with records that have also been aligned to the AICC2023 chronology.

For each of the study sites, benthic $\delta^{18}O$ ties were used primarily to define the onset of the interglacial, as this is an easily definable feature, and then RPI was used to refine millennial-scale change within the interglacial. With the exception of Site U1302, the onset and end of MIS 11c do not differ substantially from published age models.

The original age model (LR04) produced a good visual comparison between oxygen isotope records of *Nps* between U1302 and U1305; however, new % *Nps* data generated in this study, seemingly contradicts this original age model. The relative abundance of *Nps* on the original age model produces a scenario where interglacial SSTs occurred at Site U1302 during MIS 12. Given there is no other site in the North Atlantic that repeats this trend, the age model warranted re-investigation. Firstly, the records of Sites U1302 and U1305 were aligned based solely on sharp changes in *% Nps*, which produced an excellent visual match but produces exceptionally

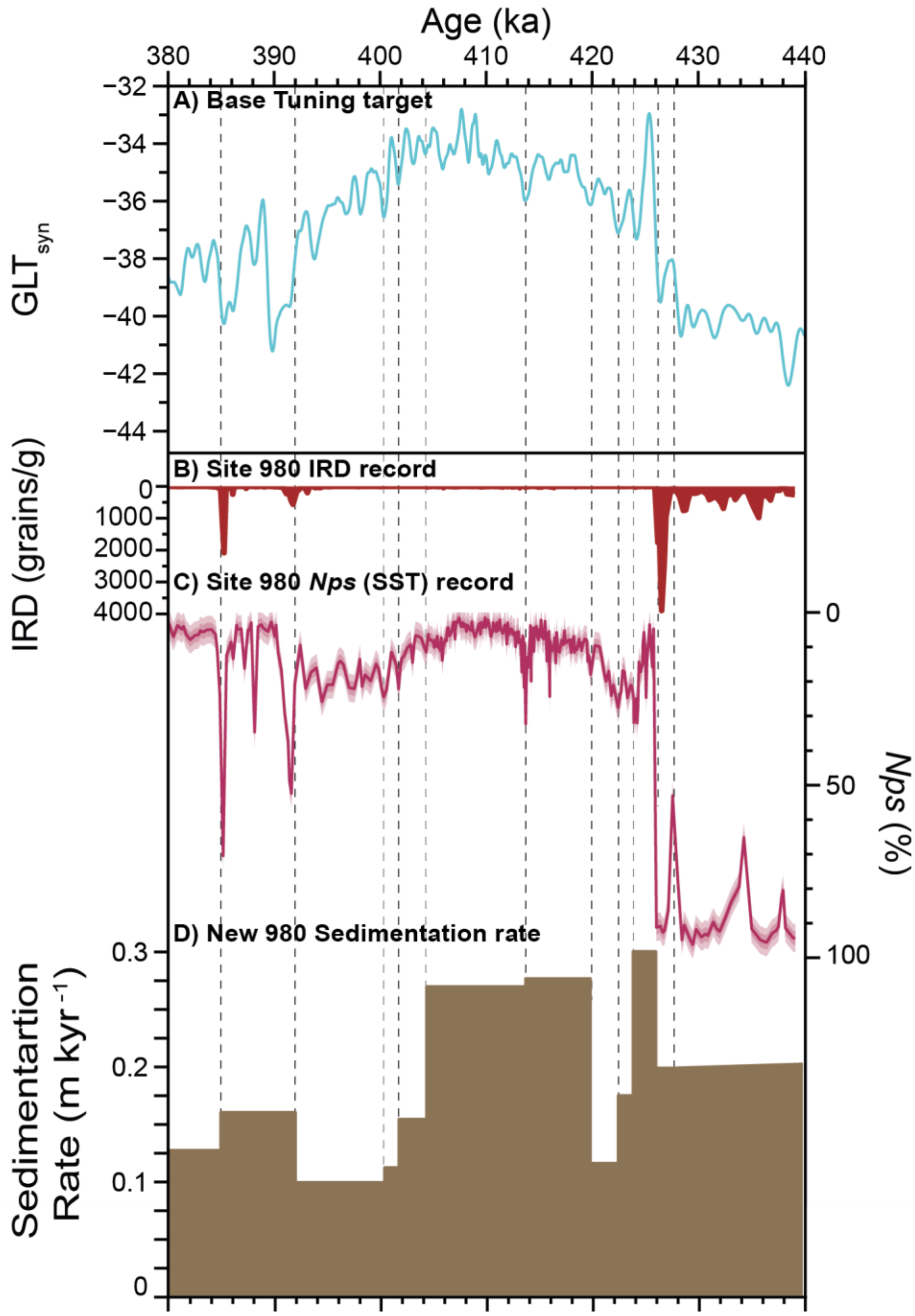

SI Figure 2: ODP Site 980 Age model on AICC23: *(**A**) GLTsyn on the AICC23 timescale ((1,18)); (B) Ice rafted debris (this study, (60)) (C) Percent Neogloboquadrina pachyderma (this study, (60)); (D) Reconstructed sedimentation rates for Site 980. Dashed black lines indicate the tie points between Site 980 Neogloboquadrina pachyderma percentages and changes in GLTsyn.*

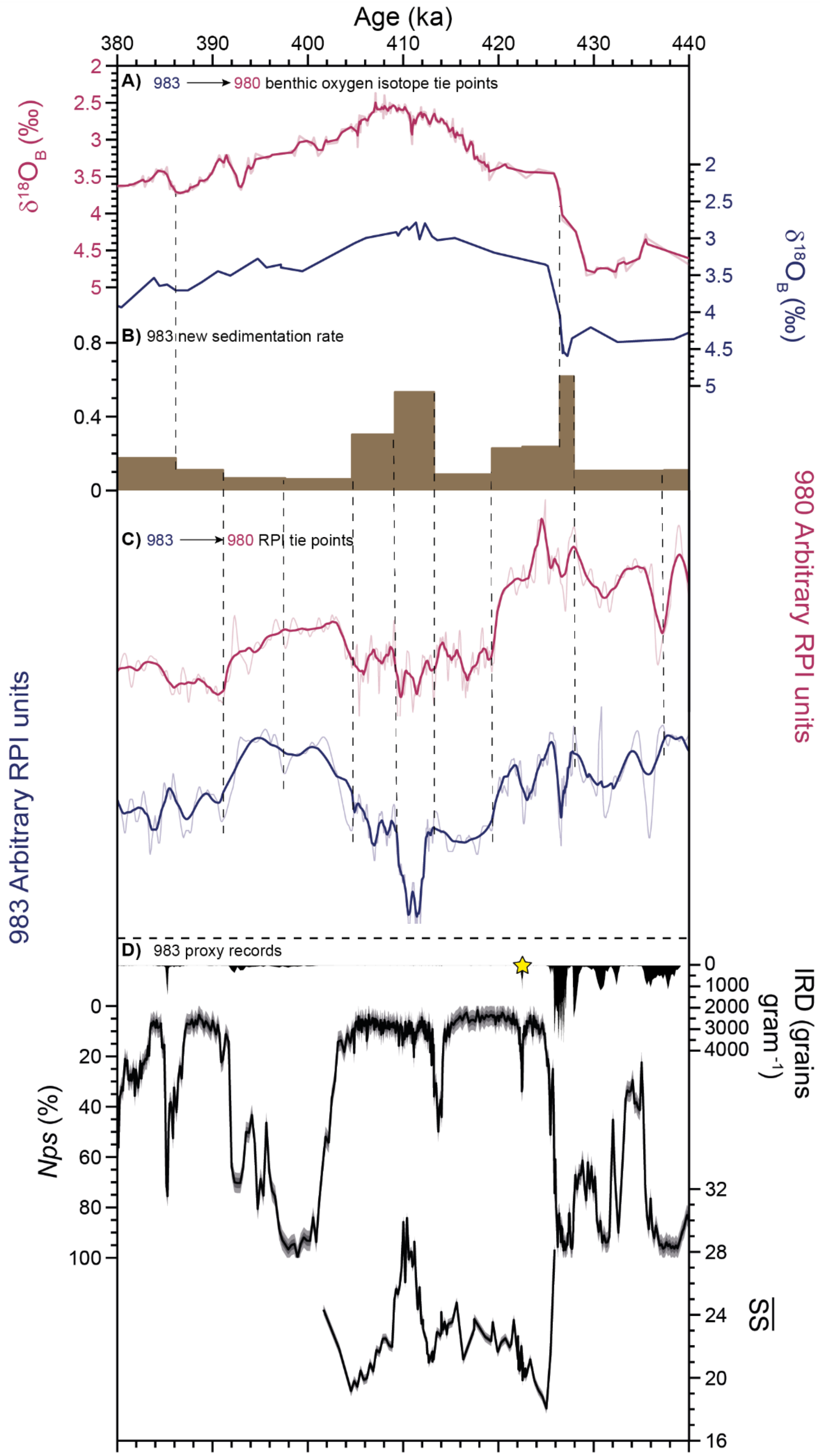
Age (ka)
380
390
400
410
420
430
440
A) 983 ——→ 980 benthic oxygen isotope tie points
δ18OB (‰)
B) 983 new sedimentation rate
C) 983 ——→ 980 RPI tie points
980 Arbitrary RPI units
983 Arbitrary RPI units
D) 983 proxy records
IRD (grains gram-1)
Nps (%)
SS

SI Figure 3: ODP Site 983 Age model on AICC23: *(**A**) Benthic oxygen isotope records of ODP Site 980 (red; this study, (60)) and ODP Site 983 (dark blue; this study, (14))**;** (**B**) Reconstructed sedimentation rates for Site 983; (**C**) RPI records for Site 980 (red; (61)) and Site 983 (dark blue; (62)); (**D**) Key site 983 proxy records on AICC2023: (top-bottom) IRD (this study; (1)), Nps (this study; (1)), mean SS (this study). Vertical dashed black lines indicate tie points between Sites 980 and 983. The yellow star indicates the timing of the terminal IRD event identified at most sites in our chronology.*

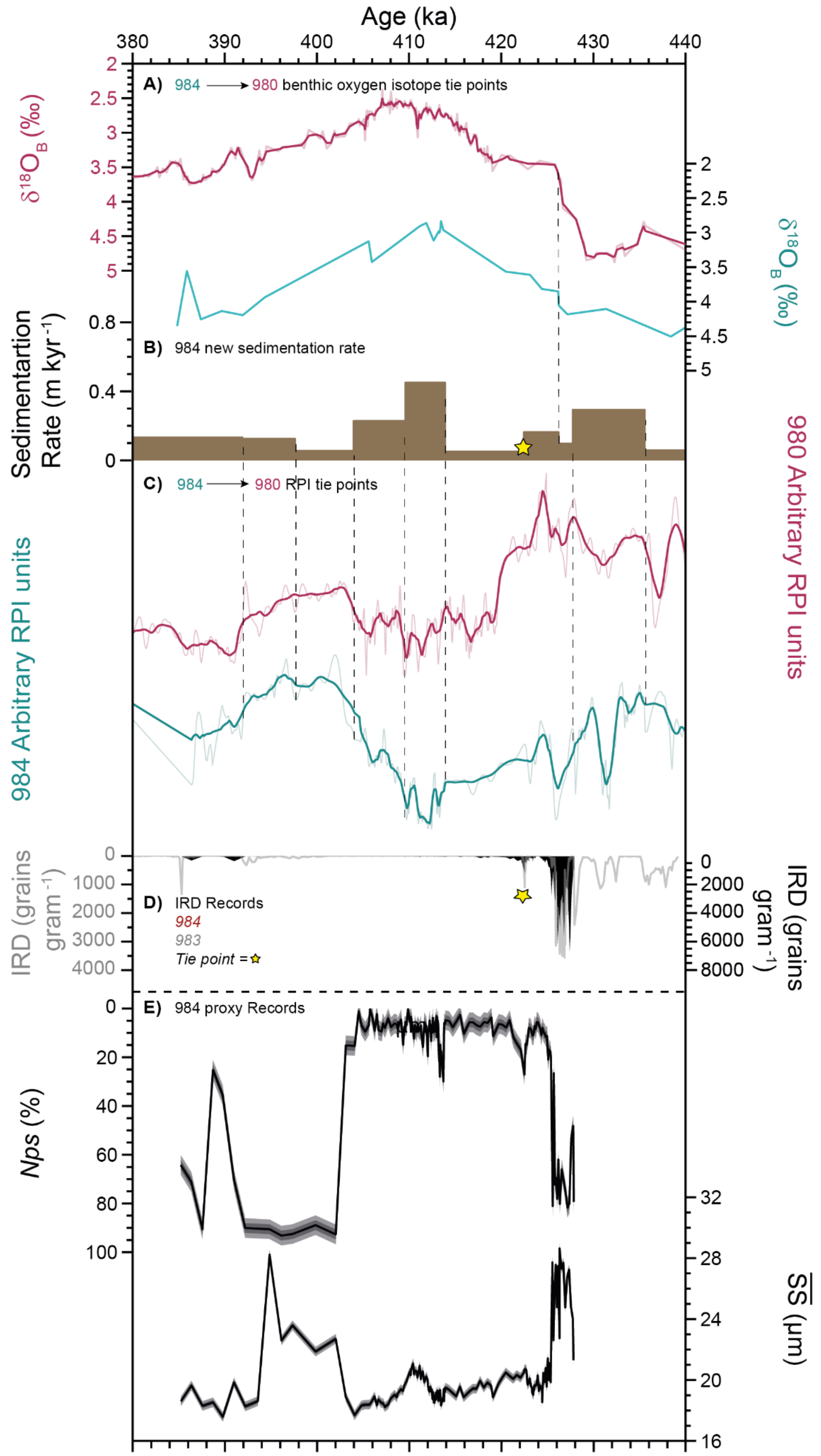
Age (ka)
380
390
400
410
420
430
440
A) 984 → 980 benthic oxygen isotope tie points
δ18OB (‰)
B) 984 new sedimentation rate
Sedimentartion Rate (m kyr-1)
0.8
0.4
0
C) 984 → 980 RPI tie points
984 Arbitrary RPI units
980 Arbitrary RPI units
D) IRD Records
984
983
Tie point =
IRD (grains gram-1)
E) 984 proxy Records
Nps (%)
SS (μm)

SI Figure 4: ODP Site 984 Age model on AICC23: *(**A**) Benthic oxygen isotope records of ODP Site 980 (red; this study, (63)) and ODP Site 984 (light blue; this study, (14)); (**B**) Reconstructed sedimentation rates for Site 984; (**C**) RPI records for Site 980 (red; (61)) and Site 984 (light blue; (64)); (**D**) Key site 984 proxy records on AICC2023: (top-bottom) IRD (this study), Nps (this study), mean SS (this study). Note that the Site 983 IRD record (this study, (1)) is superimposed in a yellow faded non-filled line for comparison. Vertical dashed black lines indicate tie points between Sites 980 and 984. The yellow star indicates the timing of the terminal IRD event identified at most sites in our chronology.*

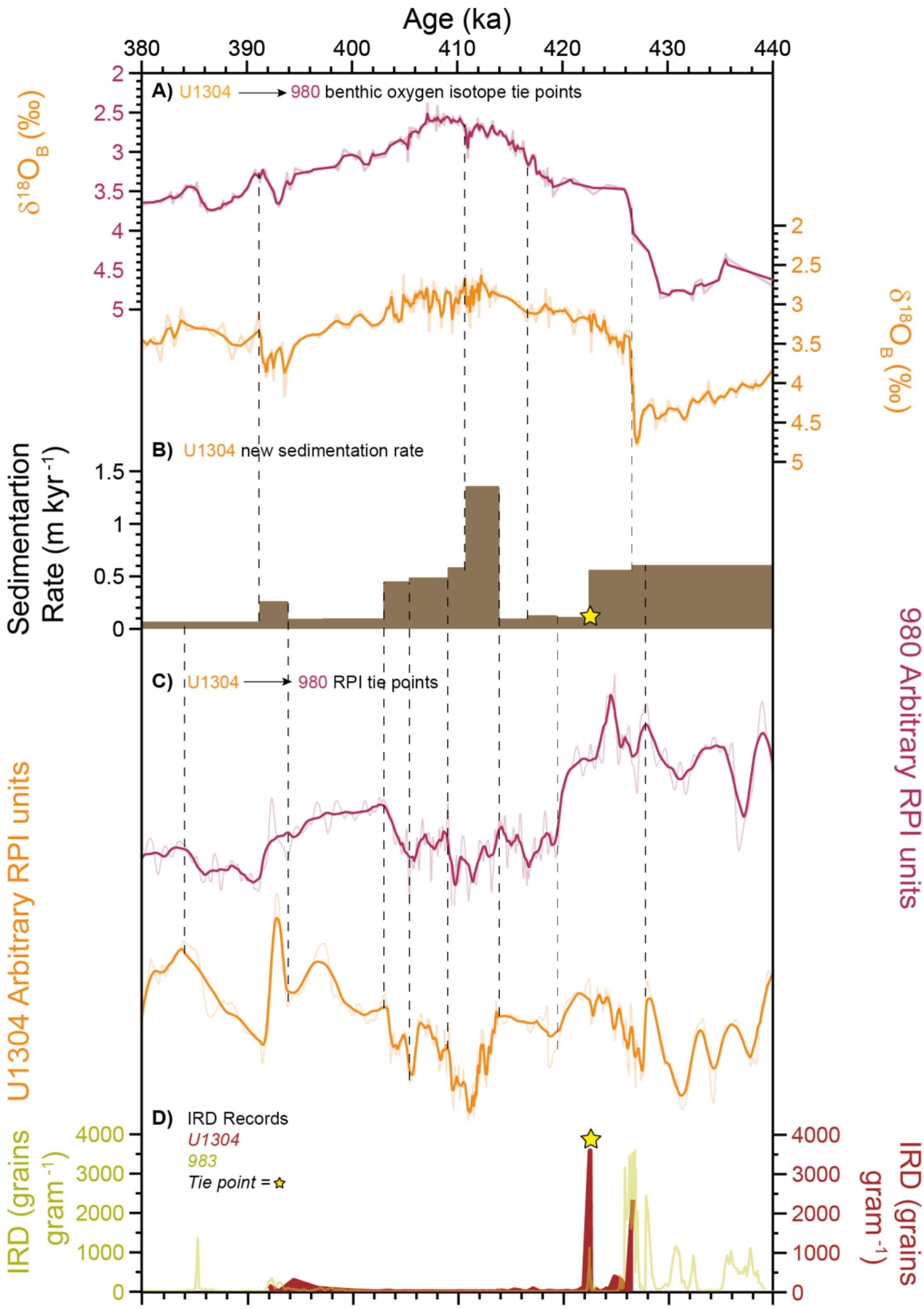
Age (ka)
380
390
400
410
420
430
440
A) U1304 → 980 benthic oxygen isotope tie points
δ18OB (‰)
B) U1304 new sedimentation rate
Sedimentartion Rate (m kyr-1)
C) U1304 → 980 RPI tie points
U1304 Arbitrary RPI units
980 Arbitrary RPI units
D) IRD Records
U1304
983
Tie point =
IRD (grains gram-1)

994

996

SI Figure 5: IODP Site U1304 Age model on AICC23: *(**A**) Benthic oxygen isotope records of ODP Site 980 (red; this study, (63)) and IODP Site U1304 (orange; this study, (15))**;** (**B**) Reconstructed sedimentation rates for Site U1304; (**C**) RPI records for Site 980 (red; (61)) and Site U1304 (orange; (15)); (**D**) Key Site U1304 proxy records on AICC2023: (top-bottom) IRD (this study), Nps (this study), mean SS (this study). Note that the Site 983 IRD record (this study, (1)) is superimposed in a yellow faded non-filled line for comparison. Vertical dashed black lines indicate tie points between Sites 980 and U1304. The yellow star indicates the timing of the terminal IRD event identified at most sites in our chronology.*

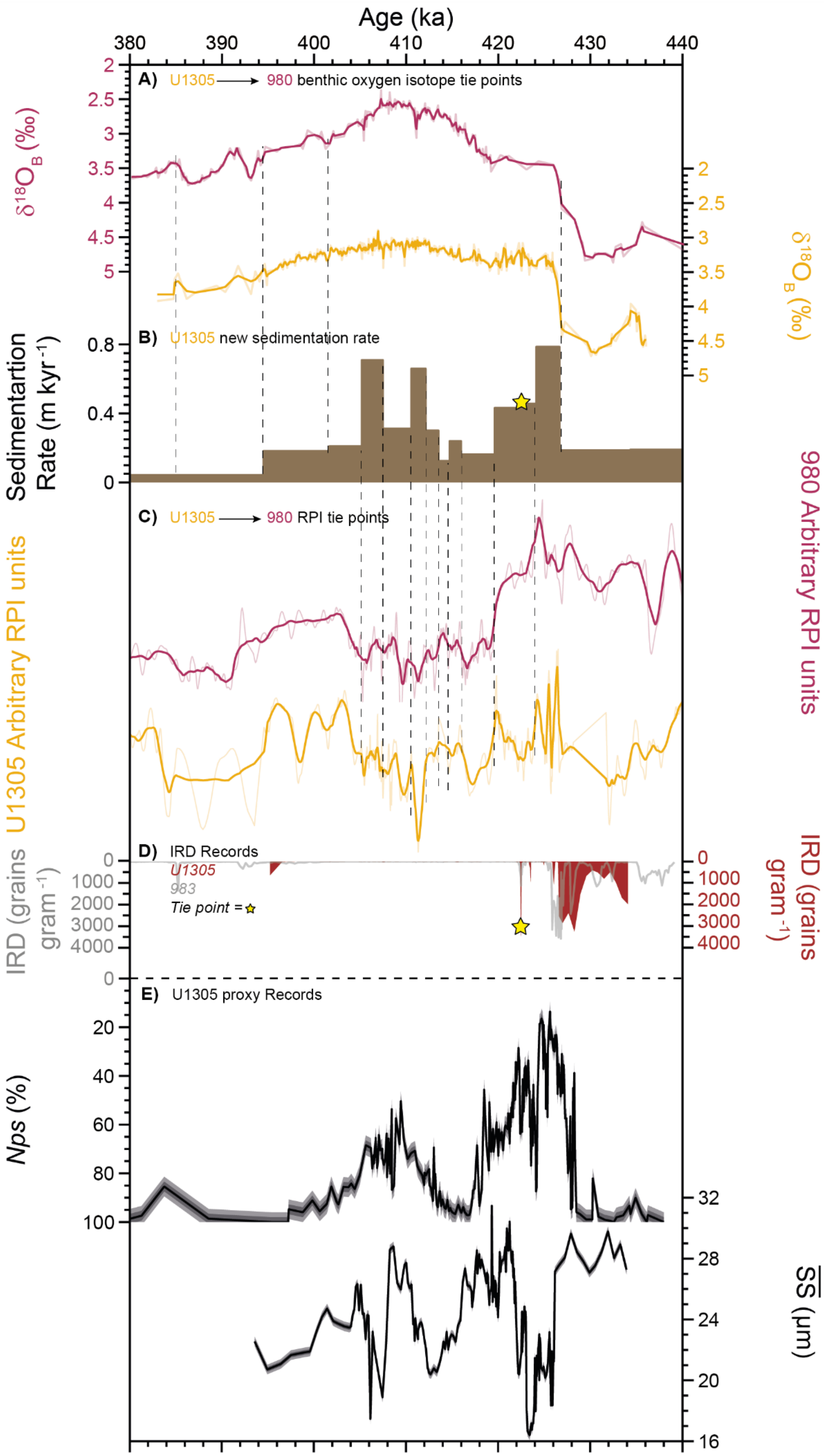

Age (ka)
380
390
400
410
420
430
440
A) U1305 → 980 benthic oxygen isotope tie points
δ18OB (‰)
B) U1305 new sedimentation rate
Sedimentartion Rate (m kyr-1)
C) U1305 → 980 RPI tie points
U1305 Arbitrary RPI units
980 Arbitrary RPI units
D) IRD Records
U1305
983
Tie point =
IRD (grains gram-1)
E) U1305 proxy Records
Nps (%)
SS (μm)

SI Figure 6: IODP Site U1305 Age model on AICC23: *(**A**) Benthic oxygen isotope records of ODP Site 980 (red; this study, (63)) and IODP Site U1305 (gold; (55))**;** (**B**) Reconstructed sedimentation rates for Site U1305; (**C**) RPI records for Site 980 (red; (61)) and Site U1305 (gold; (65)); (**D**) Key Site U1305 proxy records on AICC2023: (top-bottom) IRD (this study), Nps (this study, (43), mean SS (this study). Note that the Site 983 IRD record (this study, (1)) is superimposed in a yellow faded non-filled line for comparison. Vertical dashed black lines indicate tie points between Sites 980 and U1305. The yellow star indicates the timing of the terminal IRD event identified at most sites in our chronology.*

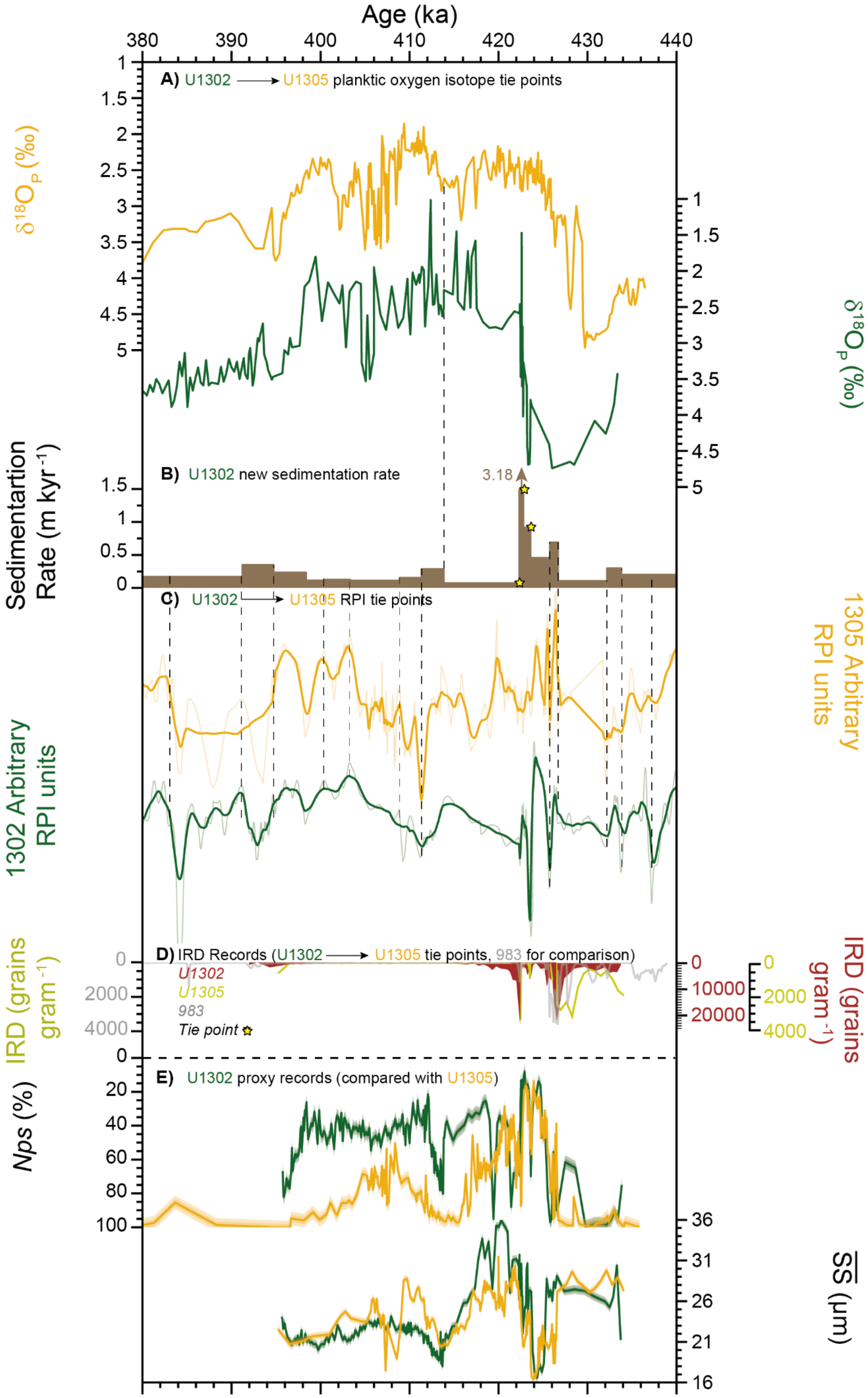
Age (ka)
380 390 400 410 420 430 440
A) U1302 → U1305 planktic oxygen isotope tie points
δ18OP (‰)
B) U1302 new sedimentation rate
3.18
Sedimentartion Rate (m kyr-1)
C) U1302 → U1305 RPI tie points
1305 Arbitrary RPI units
1302 Arbitrary RPI units
D) IRD Records (U1302 → U1305 tie points, 983 for comparison)
U1302
U1305
983
Tie point
IRD (grains gram-1)
E) U1302 proxy records (compared with U1305)
Nps (%)
SS (μm)

SI Figure 7: IODP Site U1302 Age model on AICC23: *(**A**) Planktic oxygen isotope records of IODP Site U1305 (gold; (43)) and IODP Site U1302 (green; this study, (47))**;** (**B**) Reconstructed sedimentation rates for Site U1302; (**C**) RPI records for Site U1305 (orange; (65)) and Site U1302 (green; (48)); (**D**) Key Site U1305 and U1302 proxy records on AICC2023: (top-bottom, Site U1302) IRD (this study), Nps (this study), mean SS (this study). Note that the Site 983 IRD record (this study, (1)) is superimposed in a yellow faded non-filled line for comparison. Vertical dashed black lines indicate tie points between Sites U1302 and U1305. The yellow stars indicate the timing of the terminal IRD event identified at most sites in our chronology, of which multiple tie points were generated to constrain what we believe to be a massive influx in a brief interval.*

high sedimentation rates during the earliest part of the interglacial. Furthermore, SST alone cannot validate this as a new age model as local variations in SST can occur. It is important to note that whilst % *Nps* was used to identify issues with the original age model, it has not been used to generate tie points.

To resolve this discrepancy, it was necessary to look for sedimentological evidence for a substantial change in sedimentation rate. Indeed, there are two substantial shifts in dry bulk density values at 62.25 – 60.64 MCD at Site U1302, the latter of which corresponds with a shift in a* and IRD (46). The abrupt shifts in density values indicate an increased supply of material to Site U1302 during these intervals; the IRD peak suggests iceberg activity, and the increase in a* values during the second density peak suggest material is derived from the Hudson Bay region (48). It appears likely that a substantial amount of iceberg-derived material is deposited at Site U1302 between 62.25 – 60.64 MCD in a relatively brief period of time. The increase in a* and IRD values and lack of subsequent IRD deposition at Site U1305 following this IRD peak suggests that these two final IRD spikes at Site U1302 and Site U1305 are concurrent; consequently, tie points were generated for this. Red layers such as these have been identified as part of the 8.2 ka event and Heinrich events during the transition to MIS 5e in the Labrador sea and are thought to be related to terminal ice rafting events sourced from the Laurentide Ice Sheet (48). In summary, it appears reasonable to expect exceptionally high sedimentation rates during these events.

Following this, fifteen tie points (12 RPI, 1 $d^{18}O_p$, 2 IRD) were generated, which provide records of % *Nps*, $\overline{SS}$, and IRD that are coherent between Sites U1302 and U1305. It also generates high sedimentation rates that are associated and compatible with intervals of higher sediment bulk density. However, this revised age model results in a seemingly anomalous planktic isotope data in Site U1302 from 422 – 427 ka (SI Fig. 7A). It is considered plausible that the high sedimentation rates (up to 3.18m/kyr) and high IRD flux (>20,000 grains/g) during this final interval of ice rafting (SI Figure 7B/D) likely contained substantial amounts of reworked glacial material. Given the low planktic abundance and low % *Nps*, it is possible that the *Nps* specimens selected for isotope analysis were reworked glacial foraminifera, resulting in the anomalously heavy oxygen isotope values. The revised age model also produces low sedimentation rates between 422 and 414 ka, likely caused by the cessation of the input of deglacial meltwater and sediment input after ~ 422 ka. Because the sedimentation rate is low, the effects of bioturbation are greater; therefore, the pattern of progressively declining IRD and smoothed but heavier oxygen isotope values, which can be seen in SI Fig. 7A**,** is interpreted to be a result of bioturbation of material from the very high IRD interval below ~ 422 ka, to upwards to shallower core depths. This also would produce a smoother RPI signal as lower sedimentation rates are unable to capture high-resolution changes in magnetic field strength due to a greater lock-in depth, as is observed. Together, this produces a reasonable explanation for the discrepancy between the planktic isotope records at Sites U1302 and U1305. We note that benthic isotope data has recently been published from this site (49) which produces a change in benthic oxygen isotope values at the same depth as the planktic oxygen isotope values; however, we remain convinced by our argument that this is likely reworked glacial material for the aforementioned reasons. Regardless, the differences between the two age models pertain predominantly to the older than 422 ka interval, which is not the focus of this study. Furthermore, the records used to construct our age model for the interval of interest (400 – 422 ka) is constructed using higher resolution proxy data (RPI and new planktic oxygen isotope datapoints). It is also important to note that the severity and apparent geographical spread of this event suggests that regardless of its exact timing between age models, this was likely synchronous. We also do not examine phasing of this abrupt event beyond across proxy records from the same site.

1082 ***Table 1: Calculated uncertainties for Site 980:*** *Site 980 was tuned to GLT_{Syn} on the AICC23 chronology (15). Here, both internal (this study – AICC23) and absolute (beyond AICC23) age uncertainties have been calculated. Internal uncertainty has been attributed to half range of the tie point (~ 2σ; (47)), This has been propagated through the absolute age uncertainty of AICC12 for the interval of MIS 11c (absolute uncertainties per Site 980 age tie point generated through linear interpolation of the AICC23 absolute age uncertainty).*

980 Depth	Age tie point GLTsyn AICC2023 (ka)	Tie point Description	Range (ka)	Quarter Range (1 sigma) (ka)	AICC12 uncertainty (interpol) (1sigma) (± ka)	Propogated error absolute age (980-AICC23) (1 sigma) (± ka)
47.315	365.63	GLTsyn Rise	0.80	0.20	1.59	1.60
47.565	367.75	GLTsyn Peak	0.34	0.08	1.59	1.59
48.085	370.08	GLTsyn Peak	0.28	0.07	1.55	1.56
48.515	374.07	GLTsyn Rise	0.44	0.11	1.40	1.41
48.665	375.80	GLTsyn Rise	0.64	0.16	1.31	1.32
48.715	377.71	GLTsyn Fall	0.57	0.14	1.21	1.22
49.615	384.88	GLTsyn Rise	0.33	0.08	1.11	1.12
50.735	391.96	GLTsyn shoulder	1.19	0.30	1.49	1.52
51.56	400.40	GLTSyn trough	0.48	0.12	2.12	2.12
51.71	401.75	GLTSyn trough	0.20	0.05	2.21	2.21
52.11	404.38	GLTSyn trough	0.20	0.05	2.35	2.35
54.61	413.75	GLTSyn trough	0.33	0.08	2.27	2.27
56.29	419.88	GLTSyn trough	0.32	0.08	1.79	1.80
56.59	422.51	GLTSyn trough	0.45	0.11	1.55	1.56
56.835	423.92	GLTsyn Rise	0.45	0.11	1.42	1.43
57.475	426.08	GLTSyn trough	0.53	0.13	1.25	1.26
57.78	427.63	GLTsyn Peak	0.66	0.16	1.16	1.17

1084

Table 2: Calculated uncertainties for Sites 983, 984, U1304, and U1305: *Sites 983, 984, U1304, and U1305 were tuned to Site 980 on the AICC23 chronology (15). Here, both internal (this study – AICC23) and absolute (beyond AICC23) age uncertainties have been calculated. Internal uncertainty has been attributed to half range of the tie (~ 2σ; (47)), propagated with the equivalent Site 980 error per age tie point (Site 980 uncertainties per Site age tie point generated through linear interpolation of 1σ Site 980 uncertainties). This has then further been propagated through the absolute age uncertainty of AICC23 for the interval of MIS 11c (absolute uncertainties per Site age tie point generated through linear interpolation of the AICC23 absolute age uncertainty).*

Site	Depth (MCD)	Age tie points (Site - 980) (ka)	Tie point Description	980 Uncertainty (interpol) (ka)	Tie point range (ka)	Quarter range (1 sigma) (ka)	Propogated error (Site - 980) (1 sigma) (± ka)	AICC23 uncertainty (interpol) (1sigma) (± ka)	Propogated error absolute age (Site-980-AICC23) (1sigma) (± ka)
983	39.31	362.94		0.20	0.23	0.05	0.21	1.56	1.58
983	43.37	386.13	b18O trough	0.09	2.06	0.53	0.52	1.15	1.26
983	43.92	391.09	RPI trough	0.20	0.44	0.11	0.23	1.43	1.44
983	44.35	397.62	RPI trough	0.22	0.29	0.07	0.23	1.92	1.93
983	44.78	404.63	RPI trough	0.05	0.19	0.05	0.07	2.36	2.36
983	46.14	409.13	RPI peak	0.06	0.15	0.04	0.07	2.43	2.43
983	48.33	413.24	RPI slope	0.07	0.25	0.07	0.10	2.30	2.30
983	48.86	419.31	RPI slope	0.08	0.18	0.05	0.09	1.85	1.85
983	49.59	422.51	IRD	0.10	0.27	0.08	0.12	1.55	1.56
983	50.52	426.43	Isotope slope	0.13	0.43	0.12	0.17	1.23	1.24
983	51.42	427.89	RPI	0.16	0.26	0.07	0.17	1.15	1.16
983	52.43	437.38	RPI	0.17	0.32	0.09	0.19	0.97	0.99
984	57.03	362.94	RPI trough	0.20	0.34	0.09	0.21	1.56	1.58
984	57.56	369.52	RPI trough	0.08	1.12	0.28	0.29	1.57	1.59
984	60.52	391.96	RPI slope	0.23	0.45	0.11	0.26	1.49	1.51
984	61.23	397.65	RPI Trough	0.22	0.51	0.13	0.26	1.92	1.94
984	61.58	404.04	RPI Trough	0.05	0.39	0.10	0.11	2.33	2.33
984	62.86	409.65	RPI Trough	0.06	0.26	0.07	0.09	2.42	2.42
984	64.79	413.93	RPI shoulder	0.08	0.17	0.04	0.09	2.26	2.26
984	65.22	422.51	IRD peak	0.10	0.52	0.13	0.16	1.55	1.56
984	65.83	426.25	Isotope shoulder	0.13	0.07	0.02	0.13	1.24	1.25

984	65.98	427.80	RPI peak	0.16	0.19	0.05	0.17	1.15	1.16
984	68.26	435.59	RPI trough	0.17	0.39	0.10	0.19	0.96	0.98
984	68.36	437.32	RPI peak	0.17	0.31	0.08	0.19	0.97	0.99
1304	59.27	384.00	RPI peak	0.11	0.62	0.16	0.19	1.10	1.12
1304	59.69	391.21	Isotope peak	0.21	0.64	0.16	0.26	1.43	1.46
1304	60.33	393.75	RPI trough	0.28	0.30	0.07	0.29	1.63	1.65
1304	60.62	397.16	RPI peak	0.23	0.29	0.07	0.24	1.88	1.90
1304	61.14	403.00	RPI peak	0.10	0.26	0.07	0.12	2.28	2.28
1304	62.21	405.42	RPI peak	0.05	0.31	0.08	0.09	2.38	2.38
1304	63.97	409.10	RPI peak	0.06	0.11	0.03	0.07	2.43	2.43
1304	64.95	410.80	Isotope peak	0.07	0.19	0.05	0.08	2.40	2.40
1304	69.01	413.82	RPI trough	0.08	0.18	0.05	0.09	2.27	2.27
1304	69.26	416.68	Isotope trough	0.08	0.73	0.18	0.20	2.07	2.08
1304	69.57	419.29	RPI trough	0.08	0.32	0.08	0.11	1.85	1.85
1304	69.90	422.51	IRD peak	0.10	0.89	0.22	0.24	1.55	1.57
1304	72.16	426.60	Isotope slope	0.13	0.25	0.06	0.15	1.22	1.23
1304	72.93	427.89	RPI peak	0.16	0.19	0.05	0.17	1.15	1.16
1305	64.87	385.20	Isotope peak	0.10	0.65	0.16	0.19	1.12	1.14
1305	65.27	394.51	Isotope slope	0.29	0.42	0.10	0.31	1.69	1.71
1305	66.57	401.65	Isotope slope	0.14	0.68	0.17	0.22	2.20	2.21
1305	67.31	405.18	RPI peak	0.05	0.11	0.03	0.06	2.37	2.38
1305	68.94	407.48	RPI slope	0.05	0.15	0.04	0.07	2.42	2.42
1305	69.90	410.55	RPI peak	0.06	0.19	0.05	0.08	2.40	2.41
1305	70.93	412.11	RPI slope	0.07	0.16	0.04	0.08	2.35	2.36
1305	71.35	413.51	RPI trough	0.08	0.28	0.07	0.10	2.29	2.29
1305	71.50	414.71	RPI trough	0.08	0.09	0.02	0.08	2.21	2.21
1305	71.80	415.96	RPI peak	0.08	0.19	0.05	0.09	2.13	2.13
1305	72.39	419.61	RPI slope	0.08	0.18	0.05	0.09	1.82	1.82
1305	73.64	422.51	IRD peak	0.10	0.15	0.04	0.11	1.55	1.56

1305	74.38	424.12	RPI Slope	0.11	0.29	0.07	0.13	1.40	1.41
1305	76.37	426.65	Isotope slope	0.13	0.56	0.14	0.19	1.22	1.23
1305	77.80	434.34	Isotope peak	0.17	0.78	0.19	0.26	0.97	1.01

SI Table 3: Calculated uncertainties for Site U1302: *Site U1302 was tuned to Site U1305 (after tuning Site U1305 to Site 980) on the AICC23 chronology (15). Here, both internal (this study – AICC23) and absolute (beyond AICC23) age uncertainties have been calculated. Internal uncertainty has been attributed to half range of the tie point (~ 2σ; (47)), propagated with the equivalent Site U1305 and Site U1305 error per age tie point (Site 980 and Site U1305 uncertainties per Site U1302 age tie point generated through linear interpolation of 1σ Site U1305 and Site 980 uncertainties). This has then further been propagated through the absolute age uncertainty of AICC23 for the interval of MIS 11c (absolute uncertainties per Site U1302 age tie point generated through linear interpolation of the AICC23 absolute age uncertainty).*

Site	Depth (MCD)	Age tie points (1305/1302) (ka)	Tie point Description	U1305 Uncertainty (interpol) (1 sigma) (ka)	980 Uncertainty (interpol) (1 sigma) (ka)	Range (ka)	Quarter range (1 sigma) (ka)	Propogated error (U1302 - U1305 - 980) (1 sigma) (± ka)	AICC12 uncertainty (interpol) (1sigma) (± ka)	Propogated error absolute age (U1302-980-U1305-AICC23) (1 sigma) (± ka)
U1302	54.79	383.05	RPI slope	0.16	0.12	0.17	0.04	0.21	1.10	1.12
U1302	56.16	391.24	RPI slope	0.14	0.21	0.71	0.18	0.31	1.44	1.47
U1302	57.37	394.70	RPI slope	0.12	0.29	0.11	0.03	0.31	1.70	1.73
U1302	58.22	398.35	RPI slope	0.12	0.21	0.10	0.03	0.24	1.97	1.98
U1302	58.46	400.49	RPI slope	0.14	0.16	0.17	0.04	0.22	2.12	2.14
U1302	58.81	403.32	RPI hump	0.17	0.08	0.19	0.05	0.19	2.30	2.31
U1302	59.42	408.89	RPI trough	0.03	0.06	0.19	0.05	0.08	2.43	2.43
U1302	59.8	411.37	RPI trough	0.04	0.07	0.21	0.05	0.10	2.38	2.38
U1302	60.5	413.84	Isotope step-change	0.04	0.08	0.17	0.04	0.10	2.27	2.27
U1302	61.1	422.34	IRD end	0.04	0.10	0.09	0.02	0.11	1.57	1.57
U1302	62.47	422.78	IRD start	0.04	0.10	0.22	0.05	0.12	1.53	1.53
U1302	63.2	423.57	IRD peak	0.04	0.11	0.21	0.05	0.13	1.45	1.46
U1302	64.2	425.78	RPI trough	0.10	0.12	0.09	0.02	0.16	1.27	1.28
U1302	64.81	426.66	RPI trough	0.12	0.13	0.12	0.03	0.18	1.22	1.23
U1302	65.39	432.21	RPI trough	0.18	0.17	0.16	0.04	0.25	1.01	1.04
U1302	65.86	433.79	RPI trough	0.19	0.17	0.17	0.04	0.26	0.98	1.01
U1302	66.55	437.23	RPI Trough	0.20	0.17	0.19	0.05	0.26	0.97	1.00

1.5. Additional age models used for comparison sites

The age models for comparison sites presented in the main text of this study are presented in SI Figure 8. These include: (A) ODP Site 1063 (33.69, -57.62; 4584m water depth); (B) ODP Site 646 (58.21, -48.37; 3460m water depth); (C) ODP Site 958 (3.25, -30.00; 3795m water depth); (D) Site MD992227 (58.21, -48.37; 3460m water depth); (E) Site MD2443 (37.89, -10.72; 292m water depth). These were generated using a series of tie points to either ODP Site 980 or to another site that had previously been tied to Site 980 on AICC2023.

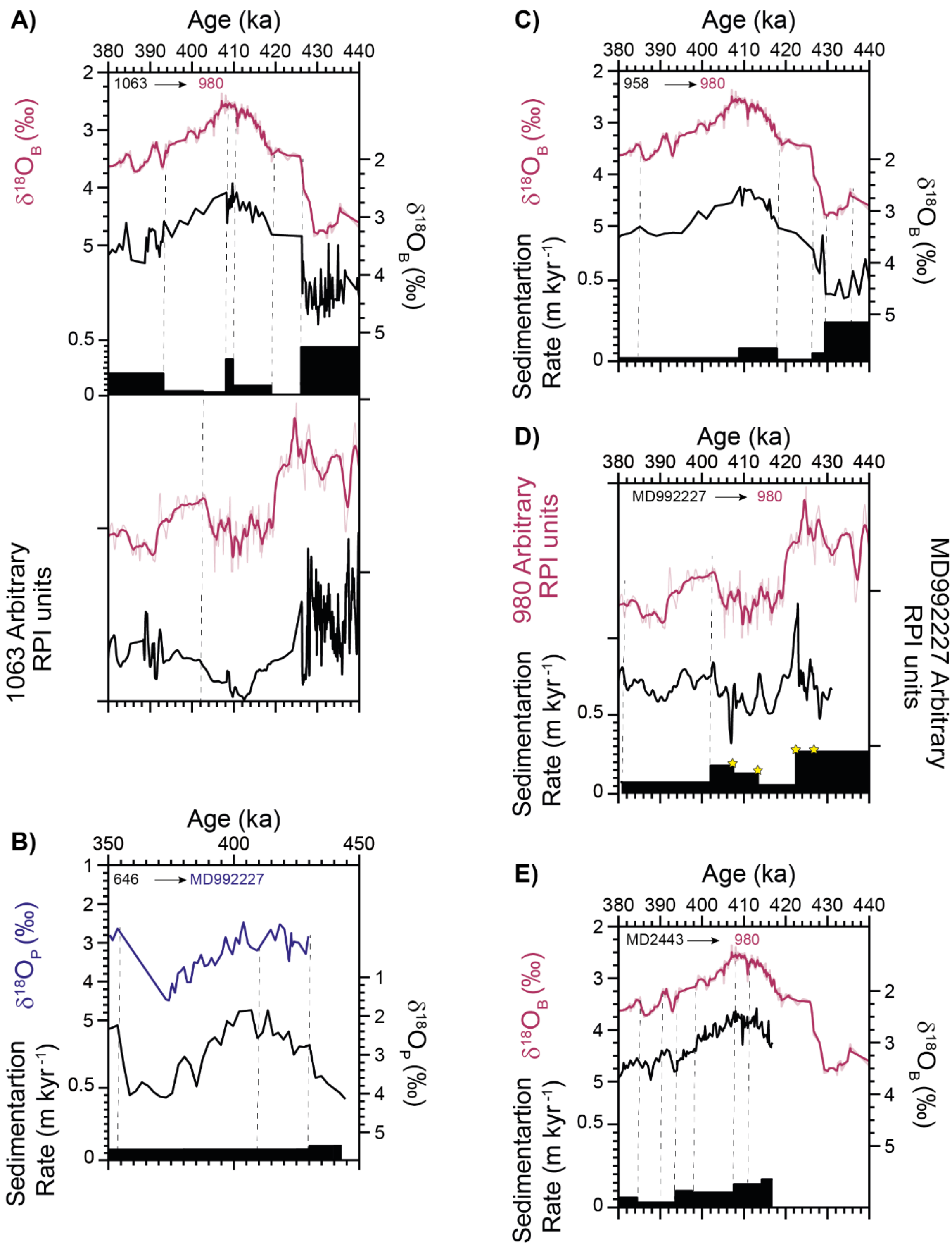

SI Figure 8: Age models for comparison sites presented in this study: (A): *Age model tie points for ODP Site 1063. (top – bottom): Benthic oxygen isotope record for Sites 980 (red;, (60) and 1063 (black,(66)); reconstructed sedimentation rates for Site 1063; RPI records for Site 980 (red; (61)) and 1063 (black,(67));* ***(B)****: Age model tie points for ODP Site 646. Note this has been tied to Site MD99-2227, which was tied to AICC2023 via Sites U1305 and 980; (top – bottom); Planktic oxygen isotope records for Sites MD99-2227 (blue; (52)) and 646 (black,(68)); reconstructed sedimentation rates. Note that due to the lower resolution of this site it has been placed on a wider (350-450 kyr) time window.* ***(C)****: Age model tie points for ODP Site 958; (top – bottom); Benthic oxygen isotope record for Sites 980 (red; (60) and 958 (black, (69)); reconstructed sedimentation rates for Site 958.* ***(D)****: Age model tie points for ODP Site MD99-2227; (top – bottom); RPI records for Sites 980 (red; (61) and MD99-2227 (black, (52)); reconstructed sedimentation rates for Site MD99-2227. Note that the gold stars indicate tie points of turbidite layers between Sites U1305 and MD99-2227 (52);* ***(E):*** *Age model tie points for Site MD01-2443; (top – bottom); Benthic oxygen isotope record for Sites 980 (red; (60) and MD01-2443 (black,(70)); reconstructed sedimentation rates for Site MD01-2443. Tie points are indicated by vertical dashed black lines.*

In the case of Site MD992227, this was primarily tied to IODP Site U1305 using the depths of co-occurring turbidite layers on Eirik Drift (50). The remaining age model tie points for study sites presented solely in the supplementary information can be found in the supplementary datasheets.

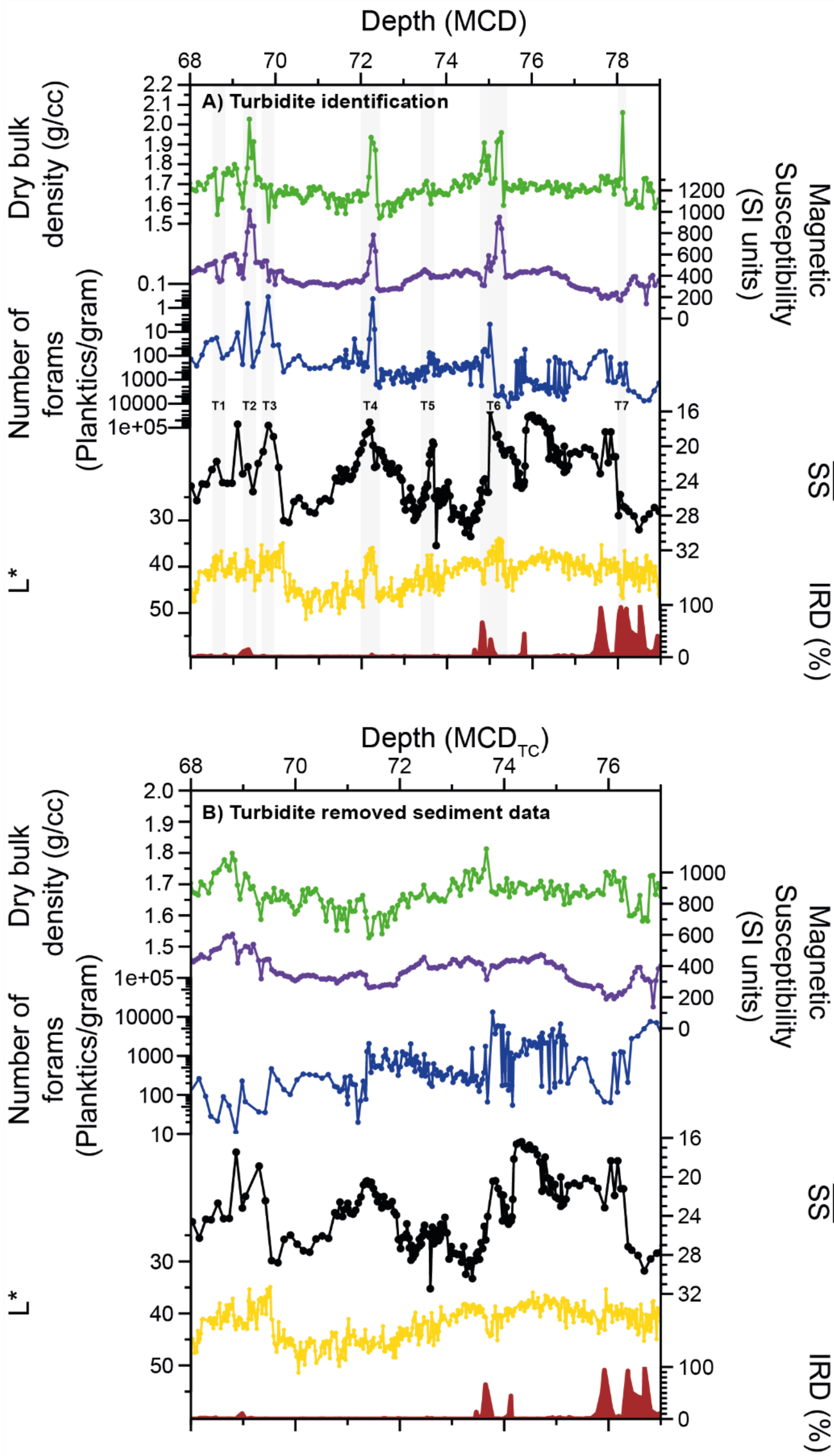
Depth (MCD)
A) Turbidite identification
Dry bulk density (g/cc)
Magnetic Susceptibility (SI units)
Number of forams (Planktics/gram)
T1
T2
T3
T4
T5
T6
T7
L*
IRD (%)
Depth (MCD_{TC})
B) Turbidite removed sediment data

SI Figure 9: Turbidite identification on Eirik Drift:* (A)** *Sediment proxy data for Dry bulk Density, Magnetic Susceptibility (71), Planktics per gram, Sortable Silt (this study), L* (71), and IRD % (this study, (43)). Turbidites are numbered according to SI Table 4 and are highlighted in grey bars. Turbidite 5 is the least certain; however, this amounts to just 15cm of sediment. Consequently, removing this as a cautious approach does not affect the overall interpretation.* ***(B) *The same sediment proxy data as in panel A but following the removal of material associated with turbidites. This is consequently plotted as Metres Composite Depth Turbidite Corrected (MCD_{TC}).*

SI Table 4 Summary of possible turbidite layers identified in IODP U1305*. MCD = Metres Composite Depth; H = High; L = Low; PG = Planktics/g; SS = Sortable Silt; BD = Bulk Density; MS = Magnetic Susceptibility; DC = Detrital Carbonate; IRD = Ice Rafted Debris.*

TURBIDITE CODE	TOP DEPTH (OLD MCD)	BOTTOM DEPTH (OLD MCD)	PROXY FEATURES	REFERENCE
T1	*68.59*	*68.84*	*LPG; LSS; LBD; LMS; LDC*	*This study*
T2	*69.24*	*69.54*	*LPG; LSS; HBD; HMS; LDC; HIRD*	(50)
T3	*69.79*	*69.89*	*LPG; LBD*	*This study*
T4	*72*	*72.38*	*LPG; LSS; HBD; HMS; LDC*	(50)
T5	*73.54*	*73.69*	*LSS; LBD; LDC*	*This study*
T6	*74.89*	*75.39*	*LPG; LSS; HBD; HMS; LDC; HIRD*	(50)
T7	*78.03*	*78.18*	*HBD; HDC*	(50)

2. Validating Nordic Seas overflow flowspeeds through the use of mean Sortable Silt

The presence of IRD can impact the reliability of the SS reconstruction. For most sites, IRD input is negligible and consistently below the 50% level suggested as likely to start impacting sortable silt (51), with the exception of the spike at ~422 ka in Sites U1304, U1305, and 984. At no point during the main interglacial period does IRD/g at ODP Site 983 exceed 50%. This suggests that there is no *a prior* reason to expect a significant impact of IRD on the sortable silt records for these sites (51), although detailed %SS vs $\overline{SS}$ for Sites 983, 984, and 1305 are available in SI Fig.8. Overall, downcore correlation of %SS vs $\overline{SS}$ for each of these sites is > 0.5 (983 = 0.95, 984 = 0.64, U1305 = 0.66). At no point do the 5-, 7-, and 9- point running correlations all drop below 0.5 for Sites 983 and 984. The same is true for site U1305 with the exception of the first 1 ka of the interglacial (425 – 424 ka).

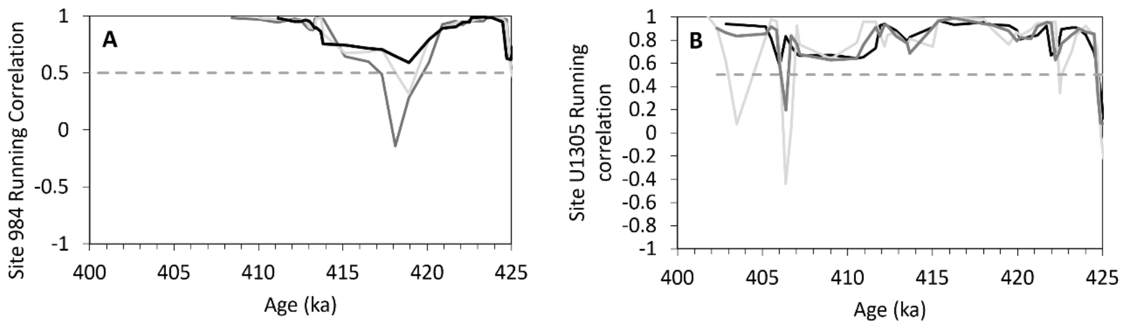

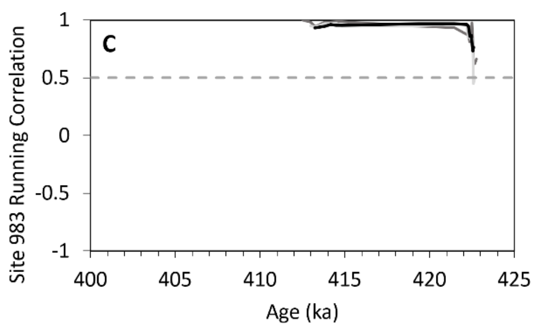

SI Figure 10: Validation of the sortable silt proxy for 3 study sites: *Following (51), the running correlation for 5 p.t (Dark Grey), 7 p.t (Light Grey), and 9 p.t (Black) averages between the mean and % sortable silt for Sites 984* ***(A)****, U1305* ***(B)****, and 983* ***(C)****. Data that is of poor quality and suited for Sortable Silt analysis is consistently below 0.5 (grey dashed line). As shown here, only brief intervals (e.g., at 422.5 ka) does the running correlation drop below 0.5. This indicates the data can be used to reconstruct deep ocean flowspeeds at these sites.*

For Site U1302 there is consistent, relatively low-level IRD input throughout most of the interglacial, but exceptionally high levels (> 20,000 grains/g) in the early stages of MIS 11c. Several samples exceed 50% IRD abundance intermittently between 417 – 434 ka, often reaching > 95%. Consequently, samples from this site were run on the Malvern to obtain downcore % $\overline{SS}$. SI Figure 11 shows that, for most of the record, there is no reason to believe the IRD is significantly impacting the $\overline{SS}$. Overall correlation between $\overline{SS}$ and % SS is high (R =0.83) whilst correlation between $\overline{SS}$ and IRD % is lower (R =0.6), which suggests that the $\overline{SS}$ record at Site U1302 is likely dominated by changes in the DWBC flow strength throughout MIS 11c (51).

Downcore correlation at 5-, 7-, and 9-point running correlations for $\overline{SS}$ vs % SS at Site U1302 do not drop below R = 0.5 with the exception of an interval from ~ 404 ka to 394 ka, and ~ 422 ka (SI Fig. 11A). For the former, values of $\overline{SS}$ are relatively low and stable at this point (average = 19.6 μm, σ = 0.76), so minor shifts in % SS (average = 32.6, σ = 2.64) could cause reduced correlation at this time without impeding the reliability of the record. For the latter, this coincides with the most extreme input of IRD at Site U1302. Consequently, data from this interval has

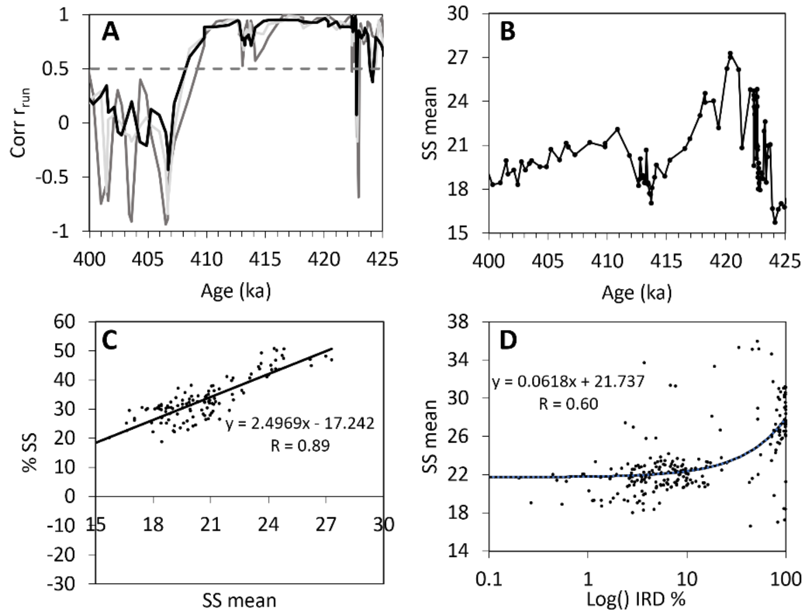

SI Figure 11: Validation of the sortable silt proxy for Site U1302: *Site U1302 contains substantially higher Ice Rafted Debris (IRD) input that other sites throughout the interglacial, but particularly between 425 and 420 ka. Whilst other sites have a maximum IRD of ~ 7000 grains per gram (e.g., Site 984), Site U1302 exceeds 20,000 grains per gram. It is therefore particularly important to assess the quality of the sortable silt record at Site U1302. (**A**)**:** Running correlations between the mean sortable silt and percentage sortable silt. Good quality data should be above 0.5 (see grey dashed line) following (51), which is the case for much of the record. (**B**): Overall downcore relationship between mean sortable silt and percentage sortable silt, which shows an excellent correlation. (**C**): The raw mean sortable silt record for Site U1302. (**D**): The correlation between sortable silt and mean sortable silt and IRD percentage, showing little change until close to ~ 70% IRD. Overall, this suggests the U1302 sortable silt record generally reflects changes in flowspeed.*

been removed from $\overline{SS}$ reconstructions for Site U1302. In summary, the overall $\overline{SS}$ record can be treated as recording changes in the DWBC.

3. Further oceanographic evidence for mid-MIS11c AMOC weakening

Previous work has used benthic $\delta^{13}C$ to infer past changes in interglacial NADW stability. In this study we rely on physically-based AMOC proxies, as opposed to geochemical proxy evidence that potentially may also be controlled by productivity and remineralisation (52). Nevertheless, when placed on our age model, we find supporting deep ocean geochemical evidence for AMOC weakening (SI Fig. 12). Both $CaCO_3$ and benthic $\delta^{13}C$ (> 3.4 km) in the deep North Atlantic decline during this event (SI Fig. 2), indicative of a reduced influence of North Atlantic Deep Water. Benthic $\delta^{13}C$ at Site U1305, which records multiple low isotopic events throughout the interglacial has been attributed to AMOC instability (53). Whilst this would support our argument, we suggest this site may not always be a reliable indicator of water mass changes due to the seasonal productivity at this site and high abundance of diatoms that may artificially lower benthic $\delta^{13}C$ (54–56). The extremely low $\delta^{13}C$ intervals at Site U1305 may possibly indicate phases of enhanced productivity caused by nutrient-rich melt from the GrIS and/or local water column stratification. Reconstruction of past seawater neodymium isotope ratios is a geochemical water mass proxy that is not affected by biological processes. Only low-resolution data exist for MIS11c, although an excursion indicating reduced NADW is recorded during mid MIS11c in the deep Northwest Atlantic (Jaume-Segui et al 20; Link 2022 PhD thesis).

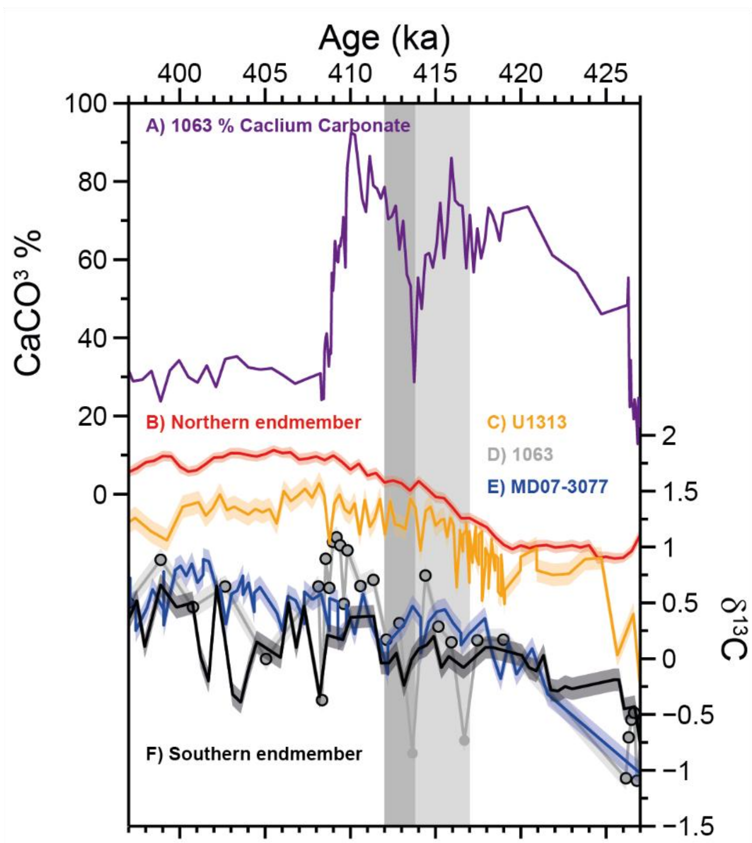

SI Figure 12: Other key Atlantic Ocean records of MIS 11c: *(**A**) AMOC$_{SPG-T}$ (this study). (**B**) AMOC$_{NSO}$ (this study). (**C**) Foram-based carbon isotope reconstructions across MIS 11c: Northern endmember calculated by averaging planktic carbon isotope data derived from N.incompta and G.inflata. Values were adjusted to G.inflata to account for species offsets. 0.4‰ was added to account changes relative to modern (69,72,73). Errors generated using a monte-carlo simulation. Benthic carbon isotope data for IODP U1304 with a $1\sigma = 0.1$‰ error (15). Benthic carbon isotope data for MD07-3077 with a $1\sigma = 0.1$‰ error (74). Southern Atlantic carbon isotope endmember (ODP 1089) with a $1\sigma = 0.1$‰ error (75).*

SI Figure captions

SI Fig. 1. Study Age model on AICC23: (**A**) Base age model generated by producing *Nps* tie points from ODP 980 (red; this study, (57)) (red triangles) to GLT_{syn} (black) on the AICC23 timescale (1,15); (**B**) Ice Rafted debris tie points at 422.5 ka for study sites. (**C**) Benthic oxygen isotope tie points for Sites U1305, U1304, 983, and 984 to ODP 980. U1302 does not presently have a published benthic oxygen isotope record. Sites 980, U1305, and U1304 have mid-weighted 3-point average solid lines with raw data as faded lines of the same colour. (**D**) Relative PalaeoIntensity tie points for Sites U1304, 984, 983, U1305, and U1302, to ODP 980. Sites are placed on a y axis reflecting arbitrary RPI units which have been scaled logarithmically (log(10)). (**E**) Reconstructed sedimentation rates for all study sites on the present age model in metres per kiloyear. Note that the highest sedimentation rate for Site U1302 is beyond the axis limit at 3.18 m/kyr. Coloured triangles indicate tie points to the base age model. These correspond to the colours used for each site. Colours: Red = ODP 980; orange = IODP U1304; yellow = IODP U1305; green = IODP U1302; dark blue = ODP 983; light blue3 = ODP 984.

SI Figure 2: ODP Site 980 Age model on AICC23: (**A**) GLTsyn on the AICC23 timescale ((1,15)); (B) Ice rafted debris (this study, (57)) (C) Percent *Neogloboquadrina pachyderma* (this study, (57)); (D) Reconstructed sedimentation rates for Site 980. Dashed black lines indicate the tie points between Site 980 *Neogloboquadrina pachyderma* percentages and changes in GLTsyn.

SI Figure 3: ODP Site 983 Age model on AICC23: (**A**) Benthic oxygen isotope records of ODP Site 980 (red; this study, (57)) and ODP Site 983 (dark blue; this study, (20))**;** (**B**) Reconstructed sedimentation rates for Site 983; (**C**) RPI records for Site 980 (red; (58)) and Site 983 (dark blue; (59)); (**D**) Key site 983 proxy records on AICC2023: (top-bottom) IRD (this study; (1)), *Nps* (this study; (1)), mean SS (this study). Vertical dashed black lines indicate tie points between Sites 980 and 983. The yellow star indicates the timing of the terminal IRD event identified at most sites in our chronology.

SI Figure 4: ODP Site 984 Age model on AICC23: (**A**) Benthic oxygen isotope records of ODP Site 980 (red; this study, (60)) and ODP Site 984 (light blue; this study, (20)); (**B**) Reconstructed sedimentation rates for Site 984; (**C**) RPI records for Site 980 (red; (58)) and Site 984 (light blue; (61)); (**D**) Key site 984 proxy records on AICC2023: (top-bottom) IRD (this study), *Nps* (this study), mean SS (this study). Note that the Site 983 IRD record (this study, (1)) is superimposed in a yellow faded non-filled line for comparison. Vertical dashed black lines indicate tie points between Sites 980 and 984. The yellow star indicates the timing of the terminal IRD event identified at most sites in our chronology.

SI Figure 5: IODP Site U1304 Age model on AICC23: (**A**) Benthic oxygen isotope records of ODP Site 980 (red; this study, (60)) and IODP Site U1304 (orange; this study, (62))**;** (**B**) Reconstructed sedimentation rates for Site U1304; (**C**) RPI records for Site 980 (red; (58)) and Site U1304 (orange; (62)); (**D**) Key Site U1304 proxy records on AICC2023: (top-bottom) IRD (this study), *Nps* (this study), mean SS (this study). Note that the Site 983 IRD record (this study, (1)) is superimposed in a yellow faded non-filled line for comparison. Vertical dashed black lines indicate tie points between Sites 980 and U1304. The yellow star indicates the timing of the terminal IRD event identified at most sites in our chronology.

SI Figure 6: IODP Site U1305 Age model on AICC23: (**A**) Benthic oxygen isotope records of ODP Site 980 (red; this study, (60)) and IODP Site U1305 (gold; (53))**;** (**B**) Reconstructed sedimentation rates for Site U1305; (**C**) RPI records for Site 980 (red; (58)) and Site U1305 (gold; (63)); (**D**) Key Site U1305 proxy records on AICC2023: (top-bottom) IRD (this study), *Nps* (this study, (41), mean SS (this study). Note that the Site 983 IRD record (this study, (1)) is superimposed in a yellow faded non-filled line for comparison. Vertical dashed black lines indicate tie points between Sites 980 and U1305. The yellow star indicates the timing of the terminal IRD event identified at most sites in our chronology.

SI Figure 7: IODP Site U1302 Age model on AICC23: (**A**) Planktic oxygen isotope records of IODP Site U1305 (gold; (41)) and IODP Site U1302 (green; this study, (45))**;** (**B**) Reconstructed sedimentation rates for Site U1302; (**C**) RPI records for Site U1305 (orange; (63)) and Site U1302 (green; (46)); (**D**) Key Site U1305 and U1302 proxy records on AICC2023: (top-bottom, Site U1302) IRD (this study), *Nps* (this study), mean SS (this study). Note that the Site 983 IRD record (this study, (1)) is superimposed in a yellow faded non-filled line for comparison. Vertical dashed black lines indicate tie points between Sites U1302 and U1305. The yellow stars indicate the timing of the terminal IRD event identified at most sites in our chronology, of which multiple tie points were generated to constrain what we believe to be a massive influx in a brief interval.

SI Figure 8: Age models for comparison sites presented in this study: (A): Age model tie points for ODP Site 1063. (top – bottom): Benthic oxygen isotope record for Sites 980 (red;, (57) and 1063 (black,(64)); reconstructed sedimentation rates for Site 1063; RPI records for Site 980 (red; (58)) and 1063 (black,(65)); **(B)**: Age model tie points for ODP Site 646. Note this has been tied to Site MD99-2227, which was tied to AICC2023 via Sites U1305 and 980; (top – bottom); Planktic oxygen isotope records for Sites MD99-2227 (blue; (50)) and 646 (black,(66)); reconstructed sedimentation rates. Note that due to the lower resolution of this site it has been placed on a wider (350-450 kyr) time window. **(C)**: Age model tie points for ODP Site 958; (top – bottom); Benthic oxygen isotope record for Sites 980 (red; (57) and 958 (black, (67)); reconstructed sedimentation rates for Site 958. **(D)**: Age model tie points for ODP Site MD99-2227; (top – bottom); RPI records for Sites 980 (red; (58) and MD99-2227 (black, (50)); reconstructed sedimentation rates for Site MD99-2227. Note that the gold stars indicate tie points of turbidite layers between Sites U1305 and MD99-2227 (50); **(E):** Age model tie points for Site MD01-2443; (top – bottom); Benthic oxygen isotope record for Sites 980 (red; (57) and MD01-2443 (black,(68)); reconstructed sedimentation rates for Site MD01-2443. Tie points are indicated by vertical dashed black lines.

SI Figure 9: Turbidite identification on Eirik Drift: (A) Sediment proxy data for Dry bulk Density, Magnetic Susceptibility (69), Planktics per gram, Sortable Silt (this study), L* (69), and IRD % (this study, (41)). Turbidites are numbered according to SI Table 4 and are highlighted in grey bars. Turbidite 5 is the least certain; however, this amounts to just 15cm of sediment.

Consequently, removing this as a cautious approach does not affect the overall interpretation. **(B)** The same sediment proxy data as in panel A but following the removal of material associated with turbidites. This is consequently plotted as Metres Composite Depth Turbidite Corrected (MCD_{TC}).

SI Figure 10: Validation of the sortable silt proxy for 3 study sites: Following (51), the running correlation for 5 p.t (Dark Grey), 7 p.t (Light Grey), and 9 p.t (Black) averages between the mean and % sortable silt for Sites 984 **(A)**, U1305 **(B)**, and 983 **(C)**. Data that is of poor quality and suited for Sortable Silt analysis is consistently below 0.5 (grey dashed line). As shown here, only brief intervals (*e.g.*, at 422.5 ka) does the running correlation drop below 0.5. This indicates the data can be used to reconstruct deep ocean flowspeeds at these sites.

SI Figure 11: Validation of the sortable silt proxy for Site U1302: Site U1302 contains substantially higher Ice Rafted Debris (IRD) input that other sites throughout the interglacial, but particularly between 425 and 420 ka. Whilst other sites have a maximum IRD of ~ 7000 grains per gram (e.g., Site 984), Site U1302 exceeds 20,000 grains per gram. It is therefore particularly important to assess the quality of the sortable silt record at Site U1302. (**A):** Running correlations between the mean sortable silt and percentage sortable silt. Good quality data should be above 0.5 (see grey dashed line) following (51), which is the case for much of the record. (**B)**: Overall downcore relationship between mean sortable silt and percentage sortable silt, which shows an excellent correlation. (**C)**: The raw mean sortable silt record for Site U1302. (**D)**: The correlation between sortable silt and mean sortable silt and IRD percentage, showing little change until close to ~ 70% IRD. Overall, this suggests the U1302 sortable silt record generally reflects changes in flowspeed.

SI Figure 12: Other key Atlantic Ocean records of MIS 11c: (**A**) $AMOC_{SPG-T}$ (this study). (**B**) $AMOC_{NSO}$ (this study). (**C**) Foram-based carbon isotope reconstructions across MIS 11c: Northern endmember calculated by averaging planktic carbon isotope data derived from *N.incompta* and *G.inflata*. Values were adjusted to *G.inflata* to account for species offsets. 0.4‰ was added to account changes relative to modern (67,70,71). Errors generated using a monte-carlo simulation. Benthic carbon isotope data for IODP U1304 with a 1σ = 0.1‰ error (62). Benthic carbon isotope data for MD07-3077 with a 1σ = 0.1‰ error (72). Southern Atlantic carbon isotope endmember (ODP 1089) with a 1σ = 0.1‰ error (73).

SI Table 1: Calculated uncertainties for Site 980: Site 980 was tuned to GLT_{Syn} on the AICC23 chronology *(15)*. Here, both internal (this study – AICC23) and absolute (beyond AICC23) age uncertainties have been calculated. Internal uncertainty has been attributed to half range of the tie point (~ 2σ; *(47)*), This has been propagated through the absolute age uncertainty of AICC12 for the interval of MIS 11c (absolute uncertainties per Site 980 age tie point generated through linear interpolation of the AICC23 absolute age uncertainty).

SI Table 2: Calculated uncertainties for Sites 983, 984, U1304, and U1305: Sites 983, 984, U1304, and U1305 were tuned to Site 980 on the AICC23 chronology *(15)*. Here, both internal (this study – AICC23) and absolute (beyond AICC23) age uncertainties have been calculated. Internal uncertainty has been attributed to half range of the tie (~ 2σ; *(47)*), propagated with the equivalent Site 980 error per age tie point (Site 980 uncertainties per Site age tie point generated through linear interpolation of 1σ Site 980 uncertainties). This has then further been propagated through the absolute age uncertainty of AICC23 for the interval of MIS 11c (absolute uncertainties per Site age tie point generated through linear interpolation of the AICC23 absolute age uncertainty).

SI Table 3: Calculated uncertainties for Site U1302: Site U1302 was tuned to Site U1305 (after tuning Site U1305 to Site 980) on the AICC23 chronology *(15)*. Here, both internal (this study – AICC23) and absolute (beyond AICC23) age uncertainties have been calculated. Internal uncertainty has been attributed to half range of the tie point (~ 2σ; *(47)*), propagated with the equivalent Site U1305 and Site U1305 error per age tie point (Site 980 and Site U1305 uncertainties per Site U1302 age tie point generated through linear interpolation of 1σ Site U1305 and Site 980 uncertainties). This has then further been propagated through the absolute age uncertainty of AICC23 for the interval of MIS 11c (absolute uncertainties per Site U1302 age tie point generated through linear interpolation of the AICC23 absolute age uncertainty).

SI Table 4: Summary of possible turbidite layers identified in IODP U1305: MCD = Metres Composite Depth; H = High; L = Low; PG = Planktics/g; SS = Sortable Silt; BD = Bulk Density; MS = Magnetic Susceptibility; DC = Detrital Carbonate; IRD = Ice Rafted Debris.

References: Supplementary Information

1. Barker S, Knorr G, Conn S, Lordsmith S, Newman D, Thornalley D. Early Interglacial Legacy of Deglacial Climate Instability. Paleoceanography and Paleoclimatology. 2019;34(8):1455–75.

2. Shimada C, Sato T, Toyoshima S, Yamasaki M, Tanimura Y. Paleoecological significance of laminated diatomaceous oozes during the middle-to-late Pleistocene, North Atlantic Ocean (IODP Site U1304). Marine Micropaleontology. 2008 Oct 1;69(2):139–50.

3. Candy I, Tye G, Coxon P, Hardiman M, Matthews I, Palmer A. A tephra-based correlation of marine and terrestrial records of MIS 11c from Britain and the North Atlantic. Journal of Quaternary Science. 2021;36(7):1149–61.

4. Caesar L, Rahmstorf S, Robinson A, Feulner G, Saba V. Observed fingerprint of a weakening Atlantic Ocean overturning circulation. Nature. 2018 Apr;556(7700):191–6.

5. Hansen B, Østerhus S. North Atlantic–Nordic Seas exchanges. Progress in Oceanography. 2000 Feb 1;45(2):109–208.

6. McCave IN, Thornalley DJR, Hall IR. Relation of sortable silt grain-size to deep-sea current speeds: Calibration of the ‘Mud Current Meter.’ Deep Sea Research Part I: Oceanographic Research Papers. 2017 Sep 1;127:1–12.

7. Rahmstorf S, Box JE, Feulner G, Mann ME, Robinson A, Rutherford S, et al. Exceptional twentieth-century slowdown in Atlantic Ocean overturning circulation. Nature Clim Change. 2015 May;5(5):475–80.

8. Telford RJ, Li C, Kucera M. Mismatch between the depth habitat of planktonic foraminifera and the calibration depth of SST transfer functions may bias reconstructions. Climate of the Past. 2013 Mar 22;9(2):859–70.

9. Moffa-Sánchez P, Moreno-Chamarro E, Reynolds DJ, Ortega P, Cunningham L, Swingedouw D, et al. Variability in the Northern North Atlantic and Arctic Oceans Across the Last Two Millennia: A Review. Paleoceanography and Paleoclimatology. 2019;34(8):1399–436.

10. Muir LC, Fedorov AV. Evidence of the AMOC interdecadal mode related to westward propagation of temperature anomalies in CMIP5 models. Clim Dyn. 2017 Mar 1;48(5):1517–35.

11. Ritz SP, Stocker TF, Grimalt JO, Menviel L, Timmermann A. Estimated strength of the Atlantic overturning circulation during the last deglaciation. Nature Geosci. 2013 Mar;6(3):208–12.

12. Wharton J. Thermal structure of the Northwest Atlantic during the last 25,000 years [Internet] [PhD Thesis]. UCL (University College London); 2023 [cited 2023 Dec 21]. Available from: https://discovery.ucl.ac.uk/id/eprint/10164435/

13. Keil P, Mauritsen T, Jungclaus J, Hedemann C, Olonscheck D, Ghosh R. Multiple drivers of the North Atlantic warming hole. Nat Clim Chang. 2020 Jul;10(7):667–71.

14. Barker S, Knorr G, Edwards RL, Parrenin F, Putnam AE, Skinner LC, et al. 800,000 Years of Abrupt Climate Variability. Science. 2011 Oct 21;334(6054):347–51.

15. Bouchet M, Landais A, Grisart A, Parrenin F, Prié F, Jacob R, et al. The Antarctic Ice Core Chronology 2023 (AICC2023) chronological framework and associated timescale for the European Project for Ice Coring in Antarctica (EPICA) Dome C ice core. Climate of the Past. 2023 Nov 10;19(11):2257–86.

16. Jouzel J, Masson-Delmotte V, Cattani O, Dreyfus G, Falourd S, Hoffmann G, et al. Orbital and Millennial Antarctic Climate Variability over the Past 800,000 Years. Science. 2007 Aug 10;317(5839):793–6.

17. Stocker TF, Johnsen SJ. A minimum thermodynamic model for the bipolar seesaw. Paleoceanography [Internet]. 2003 [cited 2023 Aug 1];18(4). Available from: https://onlinelibrary.wiley.com/doi/abs/10.1029/2003PA000920

18. Austin WEN, Hibbert FD. Tracing time in the ocean: a brief review of chronological constraints (60–8 kyr) on North Atlantic marine event-based stratigraphies. Quaternary Science Reviews. 2012 Mar 12;36:28–37.

19. Kleiven H (Kikki) F, Hall IR, McCave IN, Knorr G, Jansen E. Coupled deep-water flow and climate variability in the middle Pleistocene North Atlantic. Geology. 2011 Apr 1;39(4):343–6.

20. Lisiecki LE, Raymo ME. A Pliocene-Pleistocene stack of 57 globally distributed benthic δ18O records. Paleoceanography [Internet]. 2005 [cited 2023 Jul 31];20(1). Available from: https://onlinelibrary.wiley.com/doi/abs/10.1029/2004PA001071

21. Raymo ME, Oppo DW, Flower BP, Hodell DA, McManus JF, Venz KA, et al. Stability of North Atlantic water masses in face of pronounced climate variability during the Pleistocene. Paleoceanography [Internet]. 2004 [cited 2023 Aug 1];19(2). Available from: https://onlinelibrary.wiley.com/doi/abs/10.1029/2003PA000921

22. Barker S, Chen J, Gong X, Jonkers L, Knorr G, Thornalley D. Icebergs not the trigger for North Atlantic cold events. Nature. 2015 Apr;520(7547):333–6.

23. Imbrie J, Hays JD, Martinson DG, McIntyre A, Mix AC, Morley JJ, et al. The orbital theory of Pleistocene climate: support from a revised chronology of the marine d18O record. 1984 [cited 2023 Dec 20]; Available from: https://epic.awi.de/id/eprint/41839/1/Imbrie-etal_1984.pdf

24. Karner DB, Levine J, Medeiros BP, Muller RA. Constructing a stacked benthic δ18O record. Paleoceanography. 2002;17(3):2-1-2–16.

25. Lisiecki LE, Stern JV. Regional and global benthic δ18O stacks for the last glacial cycle. Paleoceanography. 2016;31(10):1368–94.

26. Shackleton NJ, Hall MA, Pate D. 15. Pliocene stable isotope stratigraphy of Site 846. In: Proc Ocean Drill Program Sci Results [Internet]. 1995 [cited 2023 Dec 20]. p. 337–55. Available from: http://www-odp.tamu.edu/PUBLICATIONS/138_SR/VOLUME/CHAPTERS/sr138_15.pdf

27. Govin A, Capron E, Tzedakis PC, Verheyden S, Ghaleb B, Hillaire-Marcel C, et al. Sequence of events from the onset to the demise of the Last Interglacial: Evaluating strengths and limitations of chronologies used in climatic archives. Quaternary Science Reviews. 2015 Dec 1;129:1–36.

28. Bazin L, Landais A, Lemieux-Dudon B, Toyé Mahamadou Kele H, Veres D, Parrenin F, et al. An optimized multi-proxy, multi-site Antarctic ice and gas orbital chronology (AICC2012): 120–800 ka. Climate of the Past. 2013 Aug 1;9(4):1715–31.

29. Channell JET, Xuan C, Hodell DA. Stacking paleointensity and oxygen isotope data for the last 1.5 Myr (PISO-1500). Earth and Planetary Science Letters. 2009 Jun 15;283(1):14–23.

30. Guyodo Y, Valet JP. Global changes in intensity of the Earth's magnetic field during the past 800 kyr. Nature. 1999 May;399(6733):249–52.

31. Valet JP, Meynadier L, Guyodo Y. Geomagnetic dipole strength and reversal rate over the past two million years. Nature. 2005 Jun;435(7043):802–5.

32. Gubbins D, Kent DV, Laj C, La j C, Kissel C, Mazaud A, et al. North Atlantic palaeointensity stack since 75ka (NAPIS–75) and the duration of the Laschamp event. Philosophical Transactions of the Royal Society of London Series A: Mathematical, Physical and Engineering Sciences. 2000 Mar 15;358(1768):1009–25.

33. Banerjee SK, Mellema JP. A new method for the determination of paleointensity from the A.R.M. properties of rocks. Earth and Planetary Science Letters. 1974 Sep 1;23(2):177–84.

34. King JW, Banerjee SK, Marvin J. A new rock-magnetic approach to selecting sediments for geomagnetic paleointensity studies: Application to paleointensity for the last 4000 years. Journal of Geophysical Research: Solid Earth. 1983;88(B7):5911–21.

35. Levi S, Banerjee SK. On the possibility of obtaining relative paleointensities from lake sediments. Earth and Planetary Science Letters. 1976 Feb 1;29(1):219–26.

36. Tauxe L. Sedimentary records of relative paleointensity of the geomagnetic field: Theory and practice. Reviews of Geophysics. 1993;31(3):319–54.

37. Channell JET, Mazaud A, Sullivan P, Turner S, Raymo ME. Geomagnetic excursions and paleointensities in the Matuyama Chron at Ocean Drilling Program Sites 983 and 984 (Iceland Basin). Journal of Geophysical Research: Solid Earth. 2002;107(B6):EPM 1-1-EPM 1-14.

38. Roberts AP, Tauxe L, Heslop D. Magnetic paleointensity stratigraphy and high-resolution Quaternary geochronology: successes and future challenges. Quaternary Science Reviews. 2013 Feb 1;61:1–16.

39. Roberts AP, Winklhofer M. Why are geomagnetic excursions not always recorded in sediments? Constraints from post-depositional remanent magnetization lock-in modelling. Earth and Planetary Science Letters. 2004 Nov 15;227(3):345–59.

40. Hillaire-Marcel C, de Vernal A, McKay J. Foraminifer isotope study of the Pleistocene Labrador Sea, northwest North Atlantic (IODP Sites 1302/03 and 1305), with emphasis on paleoceanographical differences between its “inner” and “outer” basins. Marine Geology. 2011 Jan 15;279(1):188–98.

41. Irvalı N, Galaasen EV, Ninnemann US, Rosenthal Y, Born A, Kleiven H (Kikki) F. A low climate threshold for south Greenland Ice Sheet demise during the Late Pleistocene. Proceedings of the National Academy of Sciences. 2020 Jan 7;117(1):190–5.

42. Kuroyanagi A, Kawahata H. Vertical distribution of living planktonic foraminifera in the seas around Japan. Marine Micropaleontology. 2004 Oct 1;53(1):173–96.

43. Simstich J, Sarnthein M, Erlenkeuser H. Paired δ18O signals of Neogloboquadrina pachyderma (s) and Turborotalita quinqueloba show thermal stratification structure in Nordic Seas. Marine Micropaleontology. 2003 May 1;48(1):107–25.

44. Bé AWH, Tolderlund DS. Seasonal Distribution of Planktonic Foraminifera in the Western North Atlantic. Micropaleontology. 1971;17(3):297–329.

45. Hillaire-Marcel C. Foraminifera isotopic records… with special attention to high northern latitudes and the impact of sea-ice distillation processes. IOP Conf Ser: Earth Environ Sci. 2011 May;14(1):012009.

46. Channell JET, Hodell DA, Romero O, Hillaire-Marcel C, de Vernal A, Stoner JS, et al. A 750-kyr detrital-layer stratigraphy for the North Atlantic (IODP Sites U1302–U1303, Orphan Knoll, Labrador Sea). Earth and Planetary Science Letters. 2012 Feb 1;317–318:218–30.

47. McCave IN, Carter L, Hall IR. Glacial–interglacial changes in water mass structure and flow in the SW Pacific Ocean. Quaternary Science Reviews. 2008 Oct 1;27(19):1886–908.

48. Nicholl JAL, Hodell DA, Naafs BDA, Hillaire-Marcel C, Channell JET, Romero OE. A Laurentide outburst flooding event during the last interglacial period. Nature Geosci. 2012 Dec;5(12):901–4.

49. Kaboth-Bahr S, Bahr A, Blaser P, Voelker AHL, Lippold J, Gutjahr M, et al. Reconstruction of deep-water undercurrent variability from the outer Labrador Sea during the past 550,000 years. Quaternary Science Advances. 2025 Jan 1;17:100266.

50. Evans HF, Channell JET, Stoner JS, Hillaire-Marcel C, Wright JD, Neitzke LC, et al. Paleointensity-assisted chronostratigraphy of detrital layers on the Eirik Drift (North Atlantic) since marine isotope stage 11. Geochemistry, Geophysics, Geosystems [Internet]. 2007 [cited 2023 Aug 2];8(11). Available from: https://onlinelibrary.wiley.com/doi/abs/10.1029/2007GC001720

51. McCave IN, Andrews JT. Distinguishing current effects in sediments delivered to the ocean by ice. I. Principles, methods and examples. Quaternary Science Reviews. 2019 May 15;212:92–107.

52. Lynch-Stieglitz J, Valley SG, Schmidt MW. Temperature-dependent ocean–atmosphere equilibration of carbon isotopes in surface and intermediate waters over the deglaciation. Earth and Planetary Science Letters. 2019 Jan 15;506:466–75.

53. Galaasen EV, Ninnemann US, Kessler A, Irvalı N, Rosenthal Y, Tjiputra J, et al. Interglacial instability of North Atlantic Deep Water ventilation. Science. 2020 Mar 27;367(6485):1485–9.

54. Gil IM, Keigwin LD, Abrantes F. The deglaciation over Laurentian Fan: History of diatoms, IRD, ice and fresh water. Quaternary Science Reviews. 2015 Dec 1;129:57–67.

55. Hawkings JR, Wadham JL, Benning LG, Hendry KR, Tranter M, Tedstone A, et al. Ice sheets as a missing source of silica to the polar oceans. Nat Commun. 2017 Jan 25;8(1):14198.

56. Hendry KR, Huvenne VAI, Robinson LF, Annett A, Badger M, Jacobel AW, et al. The biogeochemical impact of glacial meltwater from Southwest Greenland. Progress in Oceanography. 2019 Sep 1;176:102126.

57. Oppo DW, McManus JF, Cullen JL. Abrupt Climate Events 500,000 to 340,000 Years Ago: Evidence from Subpolar North Atlantic Sediments. Science. 1998 Feb 27;279(5355):1335–8.

58. Channell JET, Raymo ME. Paleomagnetic record at ODP Site 980 (Feni Drift, Rockall) for the past 1.2 Myrs. Geochemistry, Geophysics, Geosystems [Internet]. 2003 [cited 2024 Jul 9];4(4). Available from: https://onlinelibrary.wiley.com/doi/abs/10.1029/2002GC000440

59. Channell JET, Hodell DA, Lehman B. Relative geomagnetic paleointensity and δ18O at ODP Site 983 (Gardar Drift, North Atlantic) since 350 ka. Earth and Planetary Science Letters. 1997 Dec 1;153(1):103–18.

60. McManus JF, Oppo DW, Cullen JL. A 0.5-Million-Year Record of Millennial-Scale Climate Variability in the North Atlantic. Science. 1999 Feb 12;283(5404):971–5.

61. Channell JET. Geomagnetic paleointensity and directional secular variation at Ocean Drilling Program (ODP) Site 984 (Bjorn Drift) since 500 ka: Comparisons with ODP Site 983 (Gardar Drift). Journal of Geophysical Research: Solid Earth. 1999;104(B10):22937–51.

62. Xuan C, Channell JET, Hodell DA. Quaternary magnetic and oxygen isotope stratigraphy in diatom-rich sediments of the southern Gardar Drift (IODP Site U1304, North Atlantic). Quaternary Science Reviews. 2016 Jun 15;142:74–89.

63. Mazaud A, Channell JET, Stoner JS. Relative paleointensity and environmental magnetism since 1.2Ma at IODP site U1305 (Eirik Drift, NW Atlantic). Earth and Planetary Science Letters. 2012 Dec 1;357–358:137–44.

64. Hodell DA, Charles CD, Curtis JH, Mortyn PG, Ninnemann US, Venz KA. Data report: Oxygen isotope stratigraphy of ODP Leg 177 Sites 1088, 1089, 1090, 1093, and 1094. In: Proc Ocean Drill Program Sci Results [Internet]. 2003 [cited 2023 Dec 21]. p. 1–26. Available from: http://www-odp.tamu.edu/publications/177_SR/VOLUME/CHAPTERS/SR177_09.PDF

65. Channell JET, Hodell DA, Curtis JH. ODP Site 1063 (Bermuda Rise) revisited: Oxygen isotopes, excursions and paleointensity in the Brunhes Chron. Geochemistry, Geophysics, Geosystems [Internet]. 2012 [cited 2023 Sep 27];13(2). Available from: https://onlinelibrary.wiley.com/doi/abs/10.1029/2011GC003897

66. de Vernal A, Hillaire-Marcel C. Natural Variability of Greenland Climate, Vegetation, and Ice Volume During the Past Million Years. Science. 2008 Jun 20;320(5883):1622–5.

67. Kandiano ES, Bauch HA, Fahl K, Helmke JP, Röhl U, Pérez-Folgado M, et al. The meridional temperature gradient in the eastern North Atlantic during MIS 11 and its link to the ocean–atmosphere system. Palaeogeography, Palaeoclimatology, Palaeoecology. 2012 May 15;333–334:24–39.

68. Hodell D, Crowhurst S, Skinner L, Tzedakis PC, Margari V, Channell JET, et al. Response of Iberian Margin sediments to orbital and suborbital forcing over the past 420 ka. Paleoceanography. 2013;28(1):185–99.

69. Channell JET, Sato T, Kanamatsu T, Stein R, Malone M, Alvarez-Zarikian C, et al. IODP Expeditions 303 and 306 Monitor Miocene- Quaternary Climate in the North Atlantic. Scientific Drilling. 2006 Mar 1;2:4–10.

70. Voelker AHL, Rodrigues T, Billups K, Oppo D, McManus J, Stein R, et al. Variations in mid-latitude North Atlantic surface water properties during the mid-Brunhes (MIS 9–14) and their implications for the thermohaline circulation. Climate of the Past. 2010 Aug 27;6(4):531–52.

71. Oppo DW, Lehman SJ. Mid-Depth Circulation of the Subpolar North Atlantic During the Last Glacial Maximum. Science. 1993 Feb 19;259(5098):1148–52.

72. Gottschalk J, Vázquez Riveiros N, Waelbroeck C, Skinner LC, Michel E, Duplessy JC, et al. Carbon isotope offsets between benthic foraminifer species of the genus Cibicides (Cibicidoides) in the glacial sub-Antarctic Atlantic. Paleoceanography. 2016;31(12):1583–602.

73. Hodell DA, Kanfoush SL, Venz KA, Charles CD, Sierro FJ. The Mid-Brunhes Transition in Odp Sites 1089 and 1090 (Subantarctic South Atlantic). In: Earth's Climate and Orbital Eccentricity: The Marine Isotope Stage 11 Question [Internet]. American Geophysical Union (AGU); 2003 [cited 2023 Sep 25]. p. 113–29. Available from: https://onlinelibrary.wiley.com/doi/abs/10.1029/137GM09